

Nuclear Magnetic Resonance Microscopy
Using Strong Field Gradients and Constant Time Imaging

by

Sung-Min Choi

B.S., Nuclear Engineering
Seoul National University, 1988
M.S., Nuclear Engineering
Seoul National University, 1990

Submitted to the Department of Nuclear Engineering
in Partial Fulfillment of the Requirements for the
Degree of

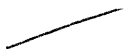
Master of Science

at the
Massachusetts Institute of Technology
February 1996

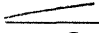
© 1996 Sung-Min Choi. All rights reserved.

The author hereby grants to MIT permission to reproduce and
to distribute publicly paper and electronic copies of this
thesis document in whole or in part.

Signature of Author _____

 Department of Nuclear Engineering
January 17, 1995

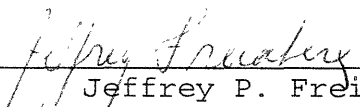
Certified by _____

 Professor
Department of Nuclear Engineering
Thesis Advisor

Certified by _____

~~Werner Maas~~, Principal Research Scientist
Bruker Inc., Billelica MA
Thesis Reader

Accepted by _____


Jeffrey P. Freidberg
Chairman, Departmental Committee on Graduate Students

MASSACHUSETTS INSTITUTE
OF TECHNOLOGY

APR 22 1996

LIBRARIES

Nuclear Magnetic Resonance Microscopy Using Strong Field Gradients and Constant Time Imaging

by

SUNG-MIN CHOI

Submitted to the Department of Nuclear Engineering
on January 17, 1995 in partial fulfillment of the
requirements for the Degree of Master of Science
in Nuclear Engineering

ABSTRACT

Nuclear magnetic resonance microscopy using strong magnetic field gradients and constant time imaging is suggested as a mean to minimize the signal attenuation due to molecular diffusion in the presence of magnetic field gradient. It is shown that the diffusive signal attenuation, which is the most important limiting factor to achieving resolution higher than $10\ \mu\text{m}$, can be significantly reduced by using strong gradients. In conventional NMR imaging techniques, however, the use of strong gradient increases the receiver bandwidth and increases the thermal noise. Constant time imaging which uses phase encoding in all directions, does not suffer this problem. The sensitivity of constant time imaging is analyzed and compared with spin echo imaging. The results show that constant time imaging provides better sensitivity than spin echo imaging especially when the diffusion effects are large.

To implement the method, a nuclear magnetic resonance microscopy probe for standard bore 400 MHz NMR spectrometer was developed and equipped with a strong gradient set (at 30 A $G_z = 1000\ \text{G/cm}$, $G_y = 1000\ \text{G/cm}$, and $G_x = 250\ \text{G/cm}$) and an efficient radiofrequency receiver. A series of images of doped water phantoms were acquired with the probe and these verify the theoretical predictions. Some biomedical samples such as rat arteries and *Drosophila melanogaster* were explored and the results show the substantial potential of NMR microscopy as a powerful tool in biomedical research.

Thesis advisor : Dr. David G. Cory
Title : Assistant Professor of Nuclear Engineering

Acknowledgments

I would like to sincerely thank Professor David G. Cory for his valuable guidance throughout this research. My sincere thanks are due to Dr. Werner Maas who has been a friend as well as a thesis reader, due to Dr. Samuel Gravina who helped so much in performing experiment during the initial stage of the research, and due to Dr. Rasesh Kapadia who provided some biological samples.

The valuable and amusing discussions with my laboratory fellows will be remembered.

I am grateful to Korean government for scholarship. This research is funded by Whitaker Foundation.

My very special thanks go to my parents, brothers, and sister.

TABLE OF CONTENTS

| | |
|--|----|
| Abstract | 2 |
| Acknowledgments | 3 |
| Chapter 1. Introduction | 6 |
| 1.1 Overview | 6 |
| 1.2 Nuclear Magnetic Resonance Phenomenon | 7 |
| Chapter 2. Principles of NMR Imaging | 13 |
| 2.1 Magnetic Field Gradient and k-space | 13 |
| 2.2 1-D, 2-D, and 3-D NMR Imaging | 15 |
| 2.3 Gradient Echo and Spin echo | 18 |
| 2.4 Slice Selection | 20 |
| Chapter 3. Fundamental Limitations to the Resolution of NMR Images | 23 |
| 3.1 Signal-to-Noise Ratio | 23 |
| 3.2 Fundamental Limitations | 25 |
| Chapter 4. Effects of Molecular Diffusion | 28 |
| 4.1 General Formalism | 28 |
| 4.2 Diffusive Signal Attenuation and Gradient Strength | 29 |
| 4.3 Diffusive Signal Attenuation in Frequency Encoding and Phase Encoding | 32 |
| 4.4 Diffusive Signal Attenuation during Slice Selection | 39 |
| Chapter 5. Constant Time Imaging | 44 |
| 5.1 General Description | 44 |
| 5.2 Sensitivity of Constant Time Imaging | 45 |
| 5.3 CPMG Sequence to Improve SNR | 53 |
| 5.4 Experiment Time of Constant Time Imaging | 55 |

| | |
|---|----|
| Chapter 6. NMR Microscopy Probe Design | 57 |
| 6.1 Strong Magnetic Field Gradient Set | 57 |
| 6.2 Sensitivity of RF Micro Coils | 62 |
| 6.3 NMR Microscopy Probe | 65 |
| Chapter 7. Representative Images and Application to Biomedical Research | 67 |
| 7.1 Images of Water Phantom | 67 |
| 7.2 Application to Biomedical Research | 73 |
| Chapter 8. Conclusion | 76 |
| References | 78 |

Chapter 1

Introduction

1.1 Overview

Since its first detection in 1946^[1-1,2] and the theoretical foundation in 1948^[1-3], Nuclear magnetic resonance (NMR) has been widely used in physics, chemistry, biology, and more recently in diagnostic medicine. A feasible procedure for NMR imaging, was proposed in 1973 by Lauterbur^[1-4], and since then numerous techniques of NMR imaging have been developed and are now commonly used in diagnostic medicine with great success.

NMR microscopy is an extension of NMR imaging with the resolution improved to a few micrometers. The idea of NMR microscopy was suggested in some of the earliest papers on NMR imaging in 1973 and 1974^[1-5,6]. It is only in recent years, however, that improvements in magnet technology have allowed its practical realization. For example, an NMR microscopic image of a single cell with a resolution $13 \times 13 \times 250 \mu\text{m}^3$, was published in Nature in 1986^[1-7].

Compared to conventional microscopy such as optical microscopy, NMR microscopy has two major advantages: first, it allows one to investigate three-dimensional information non-invasively, and second, image contrast can be based on a variety of NMR parameters such as proton density, spin-lattice relaxation times, spin-spin relaxation times, and diffusion coefficients. These provide information which is not available in conventional microscopy. However, there have been very few applications of NMR microscopy to biomedical problems precisely because, for most studies the required spatial resolution has yet to be achieved.

Given a polarizing static magnetic field strength, the attainable resolution in NMR microscopy is limited by the signal-to-noise ratio which is determined by the number of spins per a minimum volume element (voxel), molecular diffusion in the presence of magnetic field gradient, T_1 and T_2 relaxation, the chemical shift dispersion, the magnetic susceptibility and the finite sampling of k-space. Among these factors molecular diffusion, inherent to all liquid samples, is the most important limitation to resolution in NMR microscopy^[1-8,9,10,11,12]. In NMR imaging experiments, the magnetization grating for spatial encoding is generated by applying magnetic field gradients. Molecular diffusion in

the presence of the magnetic field gradient blurs the grating and reduces the signal intensity. This diffusive signal attenuation becomes very important at resolution higher 10 μm .

In the research described here, the effects of molecular diffusion in NMR microscopy are extensively analyzed and constant time imaging methods with intense short magnetic field gradients are suggested as a way of obtaining high resolution image. For the implementation of the idea, a NMR microscopy probe on a standard bore 400 MHz spectrometer was developed, which has a strong gradient set and a very efficient radio frequency receiver.

1.2 Nuclear Magnetic Resonance Phenomenon

Nuclear magnetic resonance is a quantum mechanical phenomenon in nature which is found in magnetic systems that possess both magnetic moments and angular momentum^[1-13]. All elements with a non-zero spin angular momentum have an associated magnetic moment μ ,

$$\mu = \gamma \mathbf{J}, \quad [1-1]$$

where γ is the gyromagnetic ratio and \mathbf{J} is the total angular momentum. The angular momentum is related to the dimensionless angular momentum operator \mathbf{I} by,

$$\mathbf{J} = \hbar \mathbf{I}, \quad [1-2]$$

where \hbar is Plank's constant. Both the gyromagnetic ratio, γ , and the nuclear spin, I , are inherent characteristic of each nuclear element and its state.

The nuclear spins interact with the externally applied magnetic field, \mathbf{B}_0 , by the Zeeman Hamiltonian,

$$\hat{H} = -\mu \cdot \mathbf{B}_0. \quad [1-3]$$

In a magnetic field, \mathbf{B}_0 , parallel to the z-direction, the Zeeman Hamiltonian is given by

$$\hat{H} = -\gamma \hbar B_0 I_z. \quad [1-4]$$

The eigenvalues of this Hamiltonian are multiples ($\gamma \hbar B_0$) of the eigenvalues of I_z , $m = I, I-1, \dots, -I$. Therefore the allowed energy levels are,

$$E = -\gamma \hbar B_0 m. \quad [1-5]$$

The nuclei of Hydrogen(protons) have the highest gyromagnetic ratio of stable nuclei with $\gamma = 2 \pi 4259 \text{ Hz/G}$, $I = 1/2$ and are nearly 100 % naturally abundant as well as being the main constituent of many materials. For sensitivity reasons the majority of imaging experiments are measures of the proton spin density.

For spins with $I = 1/2$, the energy levels as a function of magnetic field strength are

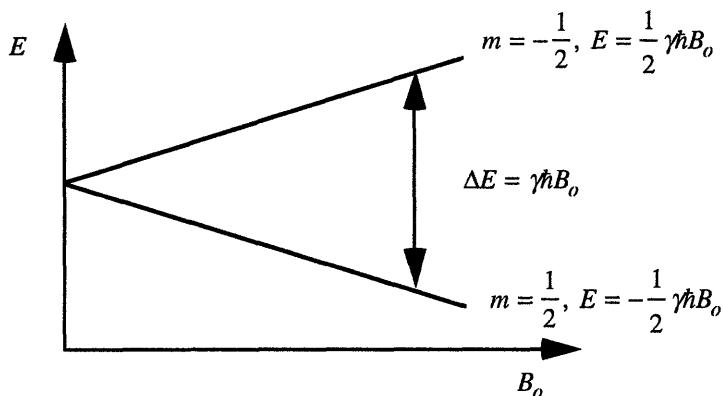


Figure 1-1. Energy levels of spins with $I = 1/2$. As the strength of magnetic field increases the splitting of the energy levels increases. Only Zeeman Hamiltonian is considered.

illustrated in Fig. 1-1. The spins of $m = +1/2$ are parallel and the spins of $m = -1/2$ are anti-parallel to the static magnetic field. The difference between the two energy levels are proportional to the gyromagnetic ratio and the external static magnetic field,

$$\Delta E = \gamma \hbar B_0 = \hbar \omega_0, \quad [1-6]$$

where

$$\omega_0 = \gamma B_0.$$

The angular frequency, ω_0 , is called Larmor frequency. At thermal equilibrium the energy levels are occupied by a collection of proton spins according to the Boltzmann distribution. The ratio of the occupation number densities of the levels is

$$\frac{N_-}{N_+} = e^{-\Delta E / k_B T}, \quad [1-7]$$

where k_B is Boltzmann's constant. The net magnetization, M_0 , of the sample at thermal equilibrium is related to the occupation number densities by

$$M_0 = \mu(N_+ - N_-). \quad [1-8]$$

To detect the existence of magnetization, an interaction that can cause transitions between the levels is required. For this purpose, an alternating magnetic field, B_1 , is applied perpendicular to the static magnetic field, which has a nonvanishing matrix element joining the two states. To satisfy the conservation of energy, the alternation frequency of the transverse B_1 field must be matched with the energy difference of the two states. This enables us to observe a resonance phenomenon. In typical static magnetic field strengths ranging from 1 T to 10 T, the resonance frequency is in the radio-frequency (RF) region. At room temperature, the population difference is about 1 spin in 10^6 and the detected magnetization is this small excess. Therefore, the NMR experiment is relatively insensitive and normally greater than 10^{15} spins are required for detection.

In the most general form, the dynamics of the bulk magnetization can be described using the density matrix since the measured bulk magnetization is from a collection of nuclear spins. For non-interacting spins with $I=1/2$, however, a semi-classical description introduced by Bloch provides a complete picture of the dynamics, and is adequate for most aspects of the imaging experiment. Therefore, only the Bloch picture is introduced here.

The dynamics of the bulk magnetization is composed of two kinds of motion, precession about the external magnetic field and relaxation back to the equilibrium state. During the RF excitation the relaxation may be neglected and the motion of the bulk magnetization is described by,

$$\frac{d}{dt}\mathbf{M}(t) = \gamma\mathbf{M}(t) \times \mathbf{B}, \quad [1-9]$$

where \mathbf{B} is a superposition of the static magnetic field along z-direction and the transverse B_1 field oscillating at the Larmor frequency. Retaining only the circularly polarized component of the oscillating B_1 field which is rotating in the same sense as the spin precession, the magnetic field \mathbf{B} is given as,

$$\mathbf{B} = B_1 \cos \omega_o t \mathbf{i} - B_1 \sin \omega_o t \mathbf{j} + B_o \mathbf{k}. \quad [1-10]$$

For the initial condition, $\mathbf{M}(t=0) = M_o \mathbf{k}$, the components of the magnetization are,

$$\begin{aligned} M_x &= M_o \sin \omega_1 t \sin \omega_o t \\ M_y &= M_o \sin \omega_1 t \cos \omega_o t, \\ M_z &= M_o \cos \omega_1 t \end{aligned} \quad [1-11]$$

where $\omega_1 = \gamma B_1$. As shown in Fig. 1-2 (a), the magnetization moves along a rather complicated path in laboratory frame, and the rotation about the B_1 field is most easily seen in rotating frame defined by the transformation,

$$\frac{d}{dt}\mathbf{M}_{rotating} = \frac{d}{dt}\mathbf{M}_{lab.} - \omega_o M_x \hat{y} + \omega_o M_y \hat{x}. \quad [1-12]$$

In this frame, the B_1 field is stationary and the magnetization undergoes a simple rotation about the B_1 field. The angle of rotation depends on the strength of the B_1 field and its duration. By varying the duration of the RF pulse with a given B_1 strength, the angle can be made equal to $\pi/2(= \omega_1 t)$ and the magnetization will be aligned along the y-axis. This is illustrated in Fig. 1-2 (b).

Once the bulk magnetization is away from equilibrium, the relaxation effects should be included to describe the dynamics. The relaxation process has two components known as spin-lattice relaxation and spin-spin relaxation. The spin-lattice relaxation process restores the thermal equilibrium magnetization M_o along the z-direction by an exchange of energy between the spin system and the surrounding thermal reservoir. This process is characterized by a time constant T_1 known as the spin-lattice relaxation time. The typical

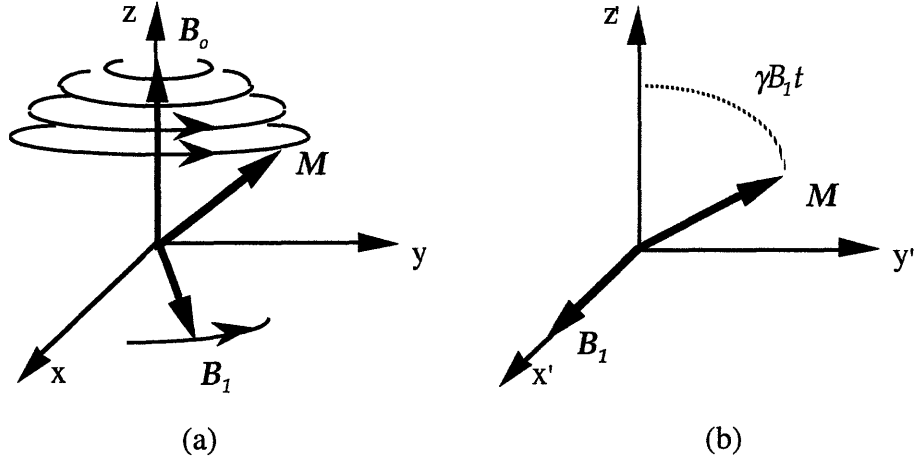


Figure 1-2. Evolution of the nuclear spin magnetization in the presence of a longitudinal field, \mathbf{B}_0 , and a transverse rotating field \mathbf{B}_1 . (a) In a laboratory frame, the magnetization follows a rather complicated path way. (b) In a rotating frame, \mathbf{B}_1 is stationary and the effective longitudinal field is zero on resonance. Only the precession about \mathbf{B}_1 is apparent.

value of T_1 is in the range 0.1 to 10 seconds for protons in dielectric liquids.

The spin-spin relaxation describes the rate of decay of the transverse magnetization and is characterized by a time constant T_2 known as the spin-spin relaxation time. In quantum mechanical term, the transverse magnetization corresponds to a state of phase coherence between the nuclear spin states. In the spin-spin relaxation process, therefore, as well as the indirect contribution of the energy exchange via the lattice, the interactions which cause the nuclear spins to dephase play a role. This makes the spin-spin relaxation time always less than the spin-lattice relaxation time.

When the relaxation processes are included, the Bloch equation describing the dynamics of a collection of non-interacting nuclear spins is,

$$\frac{d}{dt}\mathbf{M}(t) = \gamma\mathbf{M}(t) \times \mathbf{B} - \frac{1}{T_1}(M_z - M_0)\hat{z} - \frac{1}{T_2}(M_x\hat{x} + M_y\hat{y}) . \quad [1-13]$$

In a rotating frame with a static field along the z-direction and a radio frequency field along the x-direction of the frame, the Bloch equation simplifies to,

$$\begin{aligned} \frac{d}{dt}M_x &= \Delta\omega M_y - \frac{M_x}{T_2} \\ \frac{d}{dt}M_y &= -\Delta\omega M_x + \omega_1(t)M_z - \frac{M_y}{T_2} \\ \frac{d}{dt}M_z &= -\omega_1(t)M_y - \frac{(M_z - M_0)}{T_1} \end{aligned} \quad [1-14]$$

where $\Delta\omega$ is a small off-resonance frequency, the difference between the rotating frame

frequency and the Larmor frequency.

The NMR signal is measured by a tuned RF coil coupled to the sample. The transverse component of the bulk magnetization rotating about the z-axis induces an e.m.f. in the RF coil by Faraday's law and the induced e.m.f. is collected after being mixed with the output from a reference RF oscillator, a process known as heterodyning. This method of detection is inherently phase sensitive. From Eq. 1-14, the transverse components of the magnetization are obtained and, in complex notation, become,

$$M_+(t) = M_0 e^{i\Delta\omega t} e^{-t/T_2}, \quad [1-15]$$

where $M_+(t) = M_x(t) + iM_y(t)$. After the heterodyning process, the measured signal has the form,

$$S(t) = S_0 e^{i\phi} e^{i\Delta\omega t} e^{-t/T_2}, \quad [1-16]$$

where ϕ is the absolute receiver phase and S_0 is the signal immediately after the RF pulse, a number which is simply proportional to M_0 . As shown in Eq. 1-16, the NMR signal is measured in the time domain as an oscillating, decaying e.m.f. induced by the transverse magnetization during free precession. It is therefore known as the Free Induction Decay (FID). The FID can be transformed into the frequency domain by a complex Fourier transformation. When the receiver phase is zero, the real part of the frequency domain signal is a Lorentzian lineshape with a frequency offset of $\Delta\omega/2\pi$ and a full-width-half-maximum (FWHM) of $1/\pi T_2$, the so called absorption spectrum. The imaginary part of the frequency domain signal is a dispersion spectrum which has a somewhat larger width. The expression for the real part and the imaginary part of the frequency domain signal are,

$$\begin{aligned} \text{Re}\{\mathfrak{F}(S(t))\} &= \frac{T_2}{1 + (\omega - \Delta\omega)^2 T_2^2} \\ \text{Im}\{\mathfrak{F}(S(t))\} &= \frac{(\omega - \Delta\omega) T_2^2}{1 + (\omega - \Delta\omega)^2 T_2^2} \end{aligned} \quad [1-17]$$

and the FID and its complex Fourier transformation are depicted in Fig. 1-3.

Since both the Fourier transformation and the Bloch equations in the absence of an RF field are linear, we are free to break the NMR experiment into a superposition of identical experiments on each NMR distinct set of spins. So a general result is a frequency spectrum showing many resonances each corresponding to an identifiable spin system. The frequency differences may arise from small chemical shifts associated with the partial screening of the magnetic field by the electrons, from spin-spin couplings, or from local variations in the magnetic field strength due to the heterogeneity of the magnetic susceptibility throughout the sample.

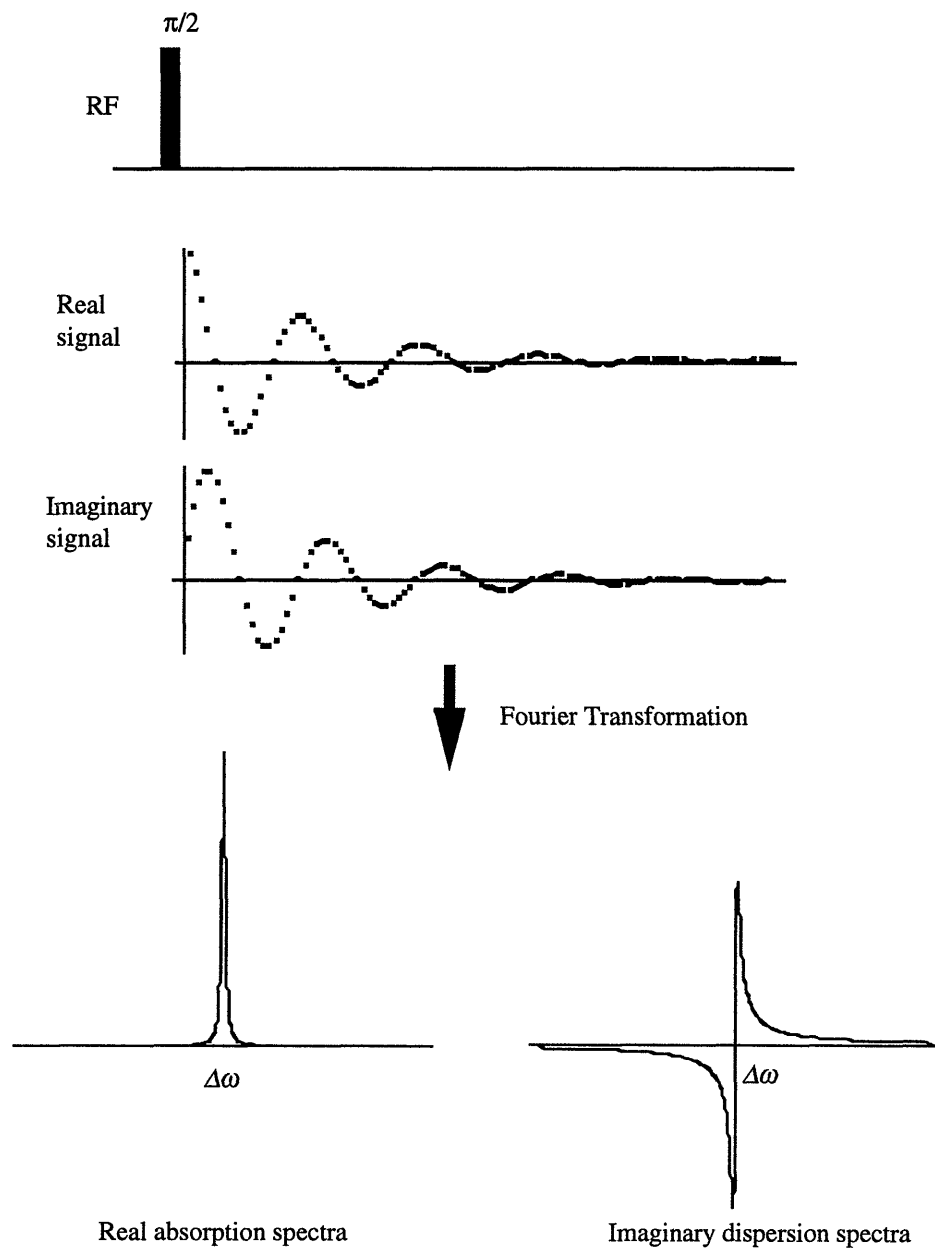


Figure 1-3. Free induction decay (FID) following a $\pi/2$ pulse and its complex Fourier transformation. The real and imaginary parts of the signal correspond to the in-phase and quadrature receiver outputs. The signal is depicted with receiver phase $\phi = 0$ and, on complex Fourier transformation, gives real absorption and imaginary dispersion spectra at the offset frequency, $\Delta\omega = \omega_o - \omega$.

Chapter 2

Principles of NMR Imaging

The purpose of all imaging experiments is to characterize the spatial heterogeneity of samples in a visible manner. NMR imaging is one of the imaging modalities, which plays a vital role in the field of clinical medicine^[2-1, 2]. NMR microscopy is an extension of NMR imaging with resolution of a few micrometers. Although the areas of application of NMR microscopy may be quite different from conventional NMR imaging, the main principles are same. NMR imaging can be classified into two broad categories, projection imaging and Fourier imaging^[2-3]. The first NMR image published in Nature by Lauterber was based on the projection reconstruction method^[2-4]. Currently however, most NMR imaging experiments use Fourier imaging and this chapter discuss only Fourier imaging.

2.1 Magnetic Field Gradient and k-Space

Since the Larmor frequency is proportional to the external static magnetic field \mathbf{B}_0 , the conventional NMR spectroscopy which extracts chemical information from the frequency spectrum requires a very homogeneous static magnetic field. In NMR imaging experiments, however, it is necessary to differentiate spins at different spatial location. For this purpose, a magnetic field which varies linearly across the sample, called magnetic field gradient, is applied. By the field gradient, the Larmor frequencies of the spins show a spatial dependence,

$$\omega(\mathbf{r}) = \gamma B_0 + \gamma \mathbf{G} \cdot \mathbf{r} \quad [2-1]$$

where \mathbf{G} is the grad of the gradient field component parallel to \mathbf{B}_0 ,

$$\mathbf{G} = \frac{\partial}{\partial x} B_z \hat{x} + \frac{\partial}{\partial y} B_z \hat{y} + \frac{\partial}{\partial z} B_z \hat{z}. \quad [2-2]$$

The simple linear relation between the Larmor frequency and the spatial coordinate \mathbf{r} of spins is the basic of the NMR imaging experiment.

In the presence of a magnetic field gradient the FID from a sample with spin density $\rho(\mathbf{r})$ is,

$$S(t) = \int \rho(\mathbf{r}) e^{i\gamma \mathbf{G} \cdot \mathbf{r} t} d\mathbf{r}, \quad [2-3]$$

where, for simplicity, the constant prefactors are set to be one and T_2 relaxation is neglected. The detected signal and the spin density are related by Fourier transformation. This can be readily seen by defining a reciprocal space vector, k , first introduced by Mansfield^[2-5,6],

$$\begin{aligned} \mathbf{k} &= \frac{1}{2\pi} \int \gamma \mathbf{G}(t) dt \\ &= \frac{1}{2\pi} \gamma \mathbf{G} t, \end{aligned} \quad [2-4]$$

where the second line of the equation is for the special case of constant gradient. The k -vector has a dimension of reciprocal space, m^{-1} , and the k -space can be traversed by moving either in time or in gradient strength. In the k -space description, the detected signal is

$$S(\mathbf{k}) = \int \rho(\mathbf{r}) e^{i2\pi\mathbf{k}\cdot\mathbf{r}} d\mathbf{r}, \quad [2-5]$$

and the spin density is obtained by inverse Fourier transformation,

$$\rho(\mathbf{r}) = \int S(\mathbf{k}) e^{-i2\pi\mathbf{k}\cdot\mathbf{r}} d\mathbf{k}. \quad [2-6]$$

Considering the constant prefactors and the T_2 relaxation, the k -space signal becomes,

$$S(\mathbf{k}, t) = S_0 e^{i\Delta\omega t} e^{-t/T_2} \int \rho(\mathbf{r}) e^{i2\pi\mathbf{k}\cdot\mathbf{r}} d\mathbf{r}. \quad [2-7]$$

Since the image is the Fourier transformation of the measured NMR signal in the presence of a magnetic field gradient, it is the spin density convoluted with the NMR lineshape in the absence of the gradient,

$$\text{Image} = \text{Spin Density} \otimes \text{NMR lineshape} + \text{Noise} \quad [2-8]$$

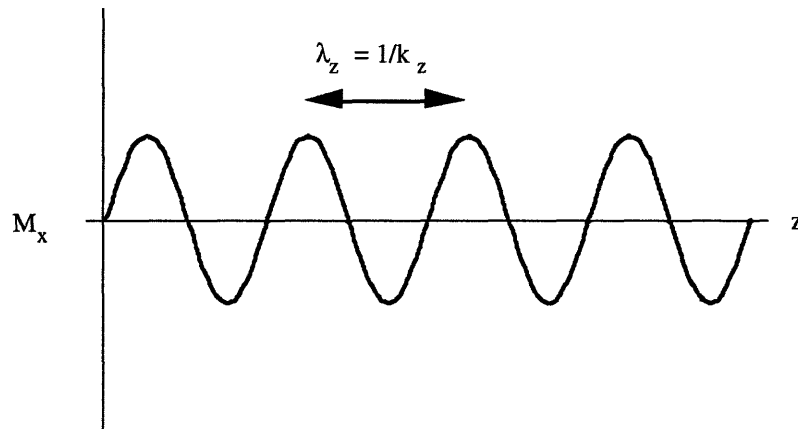


Figure 2-1. Magnetization grating induced by spatially dependent phase evolution of spins under magnetic field gradient G_z . Only real part of the transverse magnetization is shown and the sample is assumed homogeneous.

where noise is added since it exists in every experiment.

From Eq. 2-5, it is clear that the NMR imaging experiment measures the spatial frequency component of spin density. For a better practical understanding of how it works, the evolution of spins in the presence of a magnetic field gradient is considered. Spins at different spatial location evolves with different Larmor frequencies according to the magnetic field gradient. This makes the spins have a spatially dependent phase and results in a sinusoidal magnetization grating across the sample. This is illustrated in Fig. 2-1. The k-vector describes the spacing of the grating,

$$k_z = \frac{1}{\lambda_z}, \quad [2-9]$$

where λ_z is the period of the grating. In essence, by combining orthogonal gradients oriented along x, y, and z in laboratory frame, any spatial frequency component of the spin density can be measured.

2.2 1-D, 2-D, and 3-D NMR Imaging

For an NMR image, a certain range of Fourier components are necessary to reconstruct the image and in other words, a certain area of the k-space must be scanned. As shown in Eq. 2-4, the direction and the magnitude of k-vector depend on the direction and strength of the magnetic field gradients, and the duration of the gradient pulse.

Considering a 1-D k-space, we can scan it by either a frequency encoding method or by a phase encoding method, which are illustrated in Fig. 2-2. In the frequency encoding method, data are collected while the gradient is on and kept constant. Since during the data collection the k value increases continuously, the collected data correspond to sequential points in the 1-D k-space. By this method k-space is traversed parallel to the direction of the field gradient in a single excitation. In the phase encoding method, a single data is collected following each excitation after the gradient is off and this process is repeated with incrementing either the gradient strength or the gradient on-time while the other is maintained constant. Usually the gradient strength is incremented in each step while the gradient on-time is kept constant, which is called spin-warp imaging^[2-3, 7]. Fourier transformation of the collected 1-D k-space will provide a 1-D image of the sample projected perpendicular to the gradient direction.

Although both methods are essentially the same in a sense that in either way we can traverse k-space, their effects on the imaging experiment time and the quality of the image are quite different. In phase encoding, collecting N data points in k-space requires N

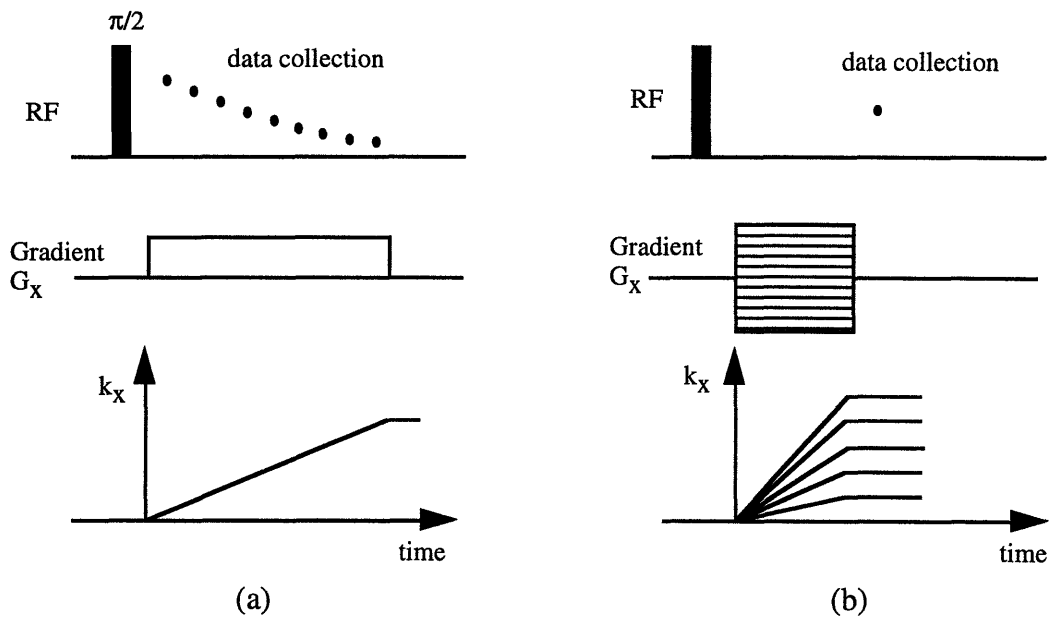


Figure 2-2. Frequency encoding and phase encoding in 1D imaging. (a) In frequency encoding data are collected while the gradient is on. A series of points in 1-D k -space is detected in a single excitation. (b) In phase encoding, a single data is collected in each excitation and in subsequent detection, the gradient strength is incremented in step while the gradient on-time is kept constant (we may increment the gradient on-time with keeping the gradient constant). Therefore the detected k -value is incremented in each excitation.

excitations while in the frequency encoding the same results can be achieved in a single excitation, so phase encoding takes longer than frequency encoding. Image distortions due to time-independent internal Hamiltonian or the inhomogeneous magnetic susceptibility may show up in the frequency encoding detection but do not in the phase encoding detection. Another difference, which is the most important factor in high resolution NMR microscopy, is found in the relative signal attenuation due to molecular diffusion. This will be extensively discussed in chapter 4.

To acquire a 2-D image, an area of 2-D k -space must be scanned. This can be achieved by using two orthogonal gradients which would work as basis vectors in 2D k -space. Since the strength and the duration of both gradients can be controlled at will, there are a variety of ways to scan 2-D k -space^[2-2, 8]. One clear way is to acquire a series of projections under various gradient orientations (which can be obtained by properly combining the two gradients) and then to use Radon filtered back projection to reconstruct the image. This is called Projection Reconstruction Imaging and early NMR images were acquired in this way. Currently, however, most imaging is performed via Fourier imaging.

A representative example is given in Fig. 2-3, in which both phase encoding and frequency encoding are used. The data are collected on a Cartesian raster in the presence of a y-gradient(frequency encoding gradient). Prior to this, a magnetization grating in the x-direction is created by a x-gradient(phase encoding gradient). Therefore, the k-vector is positioned at a certain point along k_x axis by the x-gradient and traverses along the k_y axis during the detection period. Each individual ray is collected during a separate experiment and the desired offset along the k_x axis is prepared by systematically varying the strength of the x-gradient. A 2-D Fourier transformation of the collected 2-D k-space data will return the 2-D image of sample.

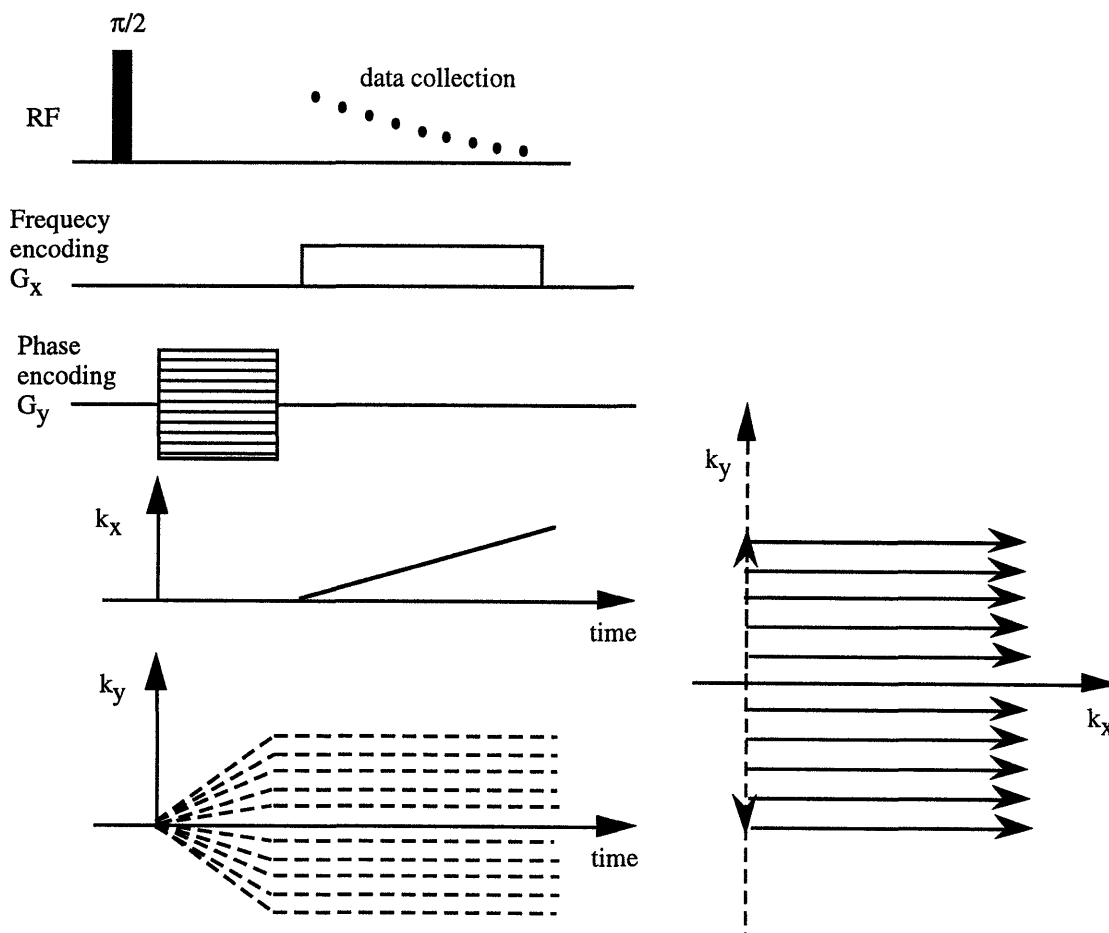


Figure 2-3. A representative 2-D Fourier imaging and its k-space trajectory. The data are collected on a Cartesian raster in the presence of a x-gradient(frequency encoding gradient). Prior to this, a magnetization grating in the y-direction is created by a y-gradient(phase encoding gradient). Therefore, the k-vector is positioned at a certain point along k_y axis by the y-gradient and traversed along k_x axis during detection period by the x-gradient. Each individual ray is collected during a separate experiment and the desired offset along the k_y axis is prepared by systematically varying the strength of y-gradient.

The extension to 3-D imaging is straight forward and can be achieved by applying another phase encoding gradient in the orthogonal direction.

2.3 Gradient-Echo and Spin-Echo

The spin dynamics are driven by the various interaction such as the chemical shift, the magnetic susceptibility, the spin-spin coupling and the magnetic field gradient. These interaction can be separated by selectively refocusing one or more interactions, which is important for the sensitivity, resolution, and contrast of images. These can be accomplished by using either RF pulses or time-dependent gradient waveform.

The gradient echo is perhaps the simplest example of this. From Eq. 2-4, we know that the k -vector which defines the periodicity of the magnetization grating, is proportional to the integrated area of the gradient waveform. Therefore, as shown in Fig. 2-4, by applying the gradient as a bi-polar pulse pair the magnetization grating is removed from the sample at the end of the gradient waveform and the spins are back in phase i.e. refocused. Since the only interaction that is influenced by the presence of a gradient is the gradient evolution itself, the gradient echo does not refocus any other interactions.

In most cases refocussing is accomplished by using RF pulses that strongly modulate the spin dynamics. RF pulses are normally arranged such that the RF field strength is stronger than any internal interaction and therefore, they can be thought of as instantaneously changing the state of the spins.

The simplest and most widely used RF pulse created echo is the spin echo which was discovered by Hahn^[2-9] and provided the key impetus to the development of pulse methods in NMR. The spin echo consist of the two pulses ($\pi/2, \pi$) shown in Fig. 2-5. The $\pi/2$ pulse rotates the magnetization from the z -axis into the transverse plane, where in the presence of a gradient it creates a magnetization grating. The π pulse inverts the phase of all the spins and this effect is equivalent to a situation in which there are no pulses, but the Hamiltonian changes its sign in time^[2-10]. Therefore the directionality of the grating is inverted and continued evolution in the magnetic filed gradient leads to the formation of echo. Since the π pulse inverts the sign of all internal Hamiltonians, the spin echo refocuses any interaction which is equivalent to a time-independent spread in magnetic fields, such as chemical shifts, heteronuclear couplings, and magnetic susceptibility shifts. One important thing to notice is that both the gradient echo and the spin echo allow one to easily access the negative portion of the frequency encoding direction in k -space.

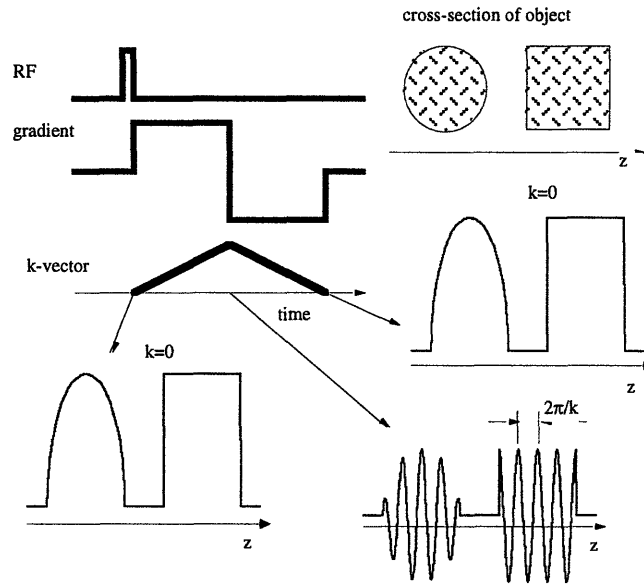


Figure 2-4. Gradient echo sequence. A gradient echo is generated by a bi-polar gradient waveform. Since the k-vector is the integrated area under the gradient waveform, at the end of the bi-polar gradient k returns to zero, and there is no magnetization grating across the sample. At the mid-point of the gradient waveform k is maximum and the grating is at its finest. Since the NMR signal is the integration of the spin magnetization across the sample, the signal maximums correspond to the two points where k is zero, and hence an echo is observed.

In the section 1.2, the spin-spin relaxation time was identified with the decay of the bulk magnetization in the transverse plane, we now see that this is not a fundamental relaxation phenomenon because, for example, the application of a magnetic field gradient can increase its rate, and because the magnetization can be refocused. The fundamental spin-spin relaxation rate is associated with those decay process that can not be refocused by the spin echo, and the observed decay of the transverse magnetization is the rate sum of this and other contributions,

$$\frac{1}{T_2^{observed}} = \frac{1}{T_2} + \frac{1}{T_2^{other}} \quad [2-10]$$

Therefore, the contrast of images will vary depending on which echo sequence is used: the spin echo will provide a contrast depending only on fundamental T_2 while the gradient echo will provide a contrast depending on the local magnetic field variation.

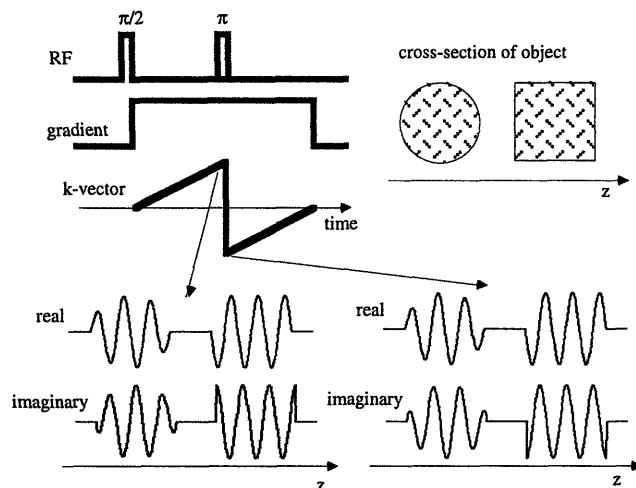


Figure 2-5. Spin echo sequence. The figure shows the actions of a π -pulse when applied to a magnetization grating. Here both quadrature components (real and imaginary) of the transverse magnetization must be kept track of. The two gratings are shown just before and just after the π -pulse which inverts the sign of one of the two components (the real component in the figure). This is consistent with the RF pulse corresponding to a rotation of 180° about an axis in the transverse plane. Before and after the π -pulse and magnetization grating has the same pitch, but the sign of the grating is changed by the pulse. Following the π -pulse the magnetic field gradient is still in the same direction and so the k-vector continues to increase, but now towards zero, and following an equal length of time k returns to zero and all of the magnetization is again coherent. A spin echo is formed.

2.4 Slice Selection

Collecting images of the whole sample may not be an efficient experiment and alternatively only one specified layer of the sample may be excited and imaged. The slice selective excitation is accomplished by using an RF pulse and a gradient together.

RF pulses can be classified as either hard or soft pulses depending on their selectivity in the NMR frequency spectrum. The bandwidth of frequencies contained in an excitation pulse is inversely proportional to the pulse duration. As shown in section 1.2, the rotation angle of a RF pulse with a duration T , is determined by the product $\gamma B_1 T$. Therefore, the bandwidth of the pulse is related to the amplitude of the transverse B_1 field. For example, a non-selective broadband $\pi/2$ pulse should have a short pulse duration and a large magnitude, B_1 , while a selective narrowband $\pi/2$ pulse should have a long pulse duration and a small B_1 . The intense broadband excitation pulses are termed hard pulses while the weak, narrowband pulses are termed soft pulses.

Since soft pulse have a narrow frequency bandwidth, they are used to selectively excite a certain chemical component which has a specific frequency spectrum. In slice

selection, the spreading of frequencies is created by the magnetic field gradient, and a certain portion of the spectrum which corresponds to a specific layer of the sample is excited by a soft pulse.

The simplest form of a soft pulse is obtained by simply reducing the amplitude and extending the duration of the usual rectangular RF pulse. This rectangular soft pulse, however, suffers from having side lobes. To reduce this problem, shaped soft pulses such as sinc modulated RF pulse are used and give reasonably well defined square frequen-

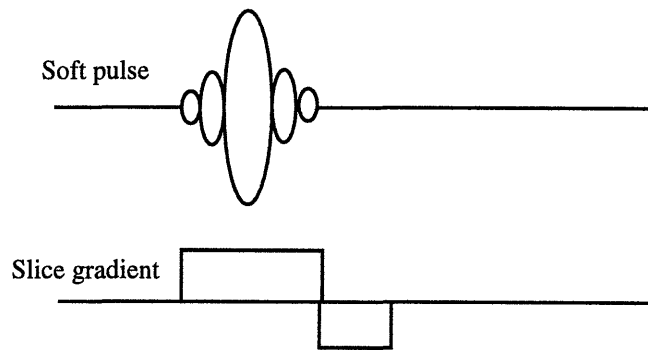


Figure 2-6. Slice selection using a sinc pulse in the presence of a magnetic field gradient. The second gradient is followed to refocus the dephasing during the first slice selection gradient.

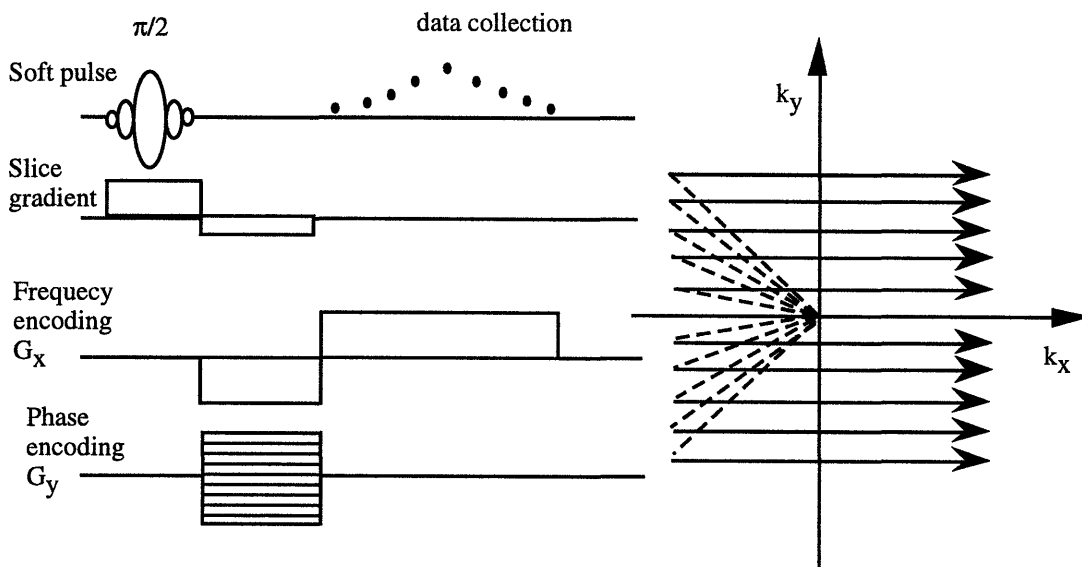


Figure 2-7. A slice selected 2-D spin warp, gradient echo sequence. During the phase encoding time the k_y vector is also offset so that both positive and negative values can be sampled.

-cy profiles. A sinc pulse in the presence of a magnetic field gradient, shown in Fig. 2-6, is the most common slice selection method in NMR imaging.

One example of a slice selected 2D gradient echo imaging is given in Fig. 2-7 which shows every main feature in NMR imaging.

Chapter 3

Fundamental Limitations to the Resolution of NMR Images

Since the advent of NMR imaging, there have been ongoing efforts to improve the spatial resolution to the subcellular level^[3-1,2,3,4,5]. However, most results were achieved in very large cells with relatively poor identification of the intrastucture of cells. For practical application of NMR microscopy in biomedical research, the spatial resolution still has to be improved. The limitations to spatial resolution are discussed in various papers^[3-6,7,8,9]. In this chapter, for proper identification of the limiting factors in the signal-to-noise ratio, a general expression of the signal-to-noise ratio is reviewed, and fundamental limiting factors to resolution is discussed.

3.1 Signal-to-Noise Ratio

The NMR signal, the oscillating e.m.f. induced in a RF coil by processing magnetization, is superimposed on the noise e.m.f. arising from random thermal motion of electrons in the RF coil, magnetically induced eddy current in the sample, and from the preamplifier. Typically, the induced e.m.f. is in the range of $10^{-9} \sim 10^{-5}$ volts and this range unfortunately includes the e.m.f. values of thermal noise^[3-10]. Therefore, the signal-to-noise ratio, the ratio of the induced e.m.f. and the noise e.m.f., is a crucial issue in NMR, especially in high resolution NMR microscopy.

The thermal equilibrium magnetization for spins $I=1/2$ was given in Eq. 1-8, which, in its most general form is,

$$M_o = N_s \hbar \gamma \text{Tr}(\rho I_z) \quad [3-1]$$

where N_s is the number of spins per unit volume and ρ is the density operator of the spin system. In the high temperature approximation^[3-11,12], the magnetization may be rewritten as,

$$M_o = N_s \hbar^2 \gamma^2 I(I+1) B_o / 3k_B T_s \quad [3-2]$$

where T_s is the sample temperature.

The transverse magnetization in complex notation is given by,

$$M_+ = M_o e^{i\omega_o t} . \quad [3-3]$$

The e.m.f. induced by this oscillating transverse magnetization following a $\pi/2$ pulse can be calculated by employing the principle of reciprocity^[3-14]. The principle of reciprocity tells us that the e.m.f. induced by a magnetic dipole moment $\mathbf{M}dV_s$ placed in a volume element dV_s at a point within the RF coil is simply related to the magnetic field (\mathbf{B}_1 / i) at that point induced by a unit current flowing in the coil. Then the induced e.m.f. i.e. the signal is described by

$$S = -(\partial / \partial t) \int_{sample} (\mathbf{B}_1 / i) \bullet \mathbf{M}dV_s . \quad [3-4]$$

From Eq. 3-3 and Eq. 3-4, the real component of the signal becomes,

$$S = \omega_o K (B_1 / i)_{xy} M_o V_s \cos \omega_o t , \quad [3-5]$$

where K is an inhomogeneity factor, $(B_1 / i)_{xy}$ is the transverse component of (\mathbf{B}_1 / i) at the center of the RF coil, and V_s is the sample volume. K and $(B_1 / i)_{xy}$ depend on the coil geometry, and for a solenoid coil K is close to 1 and $(B_1 / i)_{xy}$ is

$$(B_1 / i)_{xy} = \mu_o N_t (d^2 + L^2)^{1/2} \quad [3-6]$$

where N_t is the number of turns of a coil, d is its diameter, and L is its length.

While the sample noise is important for a large sample, it is negligible for small samples which is the usual case in NMR microscopy. The contribution from the preamplifier is hopefully very small compared to the thermal noise from a RF coil. Therefore, the thermal noise from a RF coil should be the main source of noise in NMR microscopy. In this section only the thermal noise from the RF coil is considered.

The root mean square thermal noise e.m.f. in the time domain^[3-10] is given by

$$V_{noise} = \sqrt{4k_B T_c \Delta f R} \quad [3-7]$$

where T_c is the coil temperature, R is the resistance of the coil and Δf is the detection bandwidth. At NMR frequencies (~MHz), the current in a wire is confined to a skin depth thickness^[3-13] on the wire surface so that the effective resistance of straight cylindrical wire is,

$$R = \frac{l}{p} (\mu_r \mu_o \omega_o \rho(T_c) / 2)^{1/2} , \quad [3-8]$$

where l is the length of the wire, p its circumference, μ_r its relative permeability, μ_o the permeability of vacuum, ω_o the angular frequency of current, $\rho(T_c)$ the resistivity of wire which is a function of temperature. If there are many wires in close proximity, as is the case with a RF coil, the magnetic field created by the current of one conductor influences

the distribution of current in another. This effect, the so called proximity effect, tends to reduce the surface area over which current is flowing, and the resistance is thus increased by a factor ζ . The calculation of the proximity factor is not simple, but has been carried out for a single-layer solenoid^[3-15].

The signal-to-noise ratio available following a $\pi/2$ pulse, (peak signal)/(r.m.s noise), can be obtained from Eq. 3-5, 3-7, and 3-8,

$$\frac{S_o}{V_{noise}} = \frac{KV_s(B_1/i)_{xy} N_s \gamma \hbar^2 I(I+1)}{5.05 k_B T_s} \left(\frac{p}{k_B T_c \zeta} \right)^{1/2} \frac{\omega_o^{7/4}}{[\mu\mu_o\rho(T_c)]^{1/4}}. \quad [3-9]$$

From this we notice that the signal-to-noise ratio depends on $\omega_o^{7/4}$, which implies that higher static magnetic fields are strongly recommended for NMR microscopy. For different nuclei at the same static magnetic field the dependence is $N_s \gamma^{11/4} I(I+1)$. Therefore, protons, which are the most abundant in most samples and have the largest gyromagnetic ratio of stable nuclei, are the favored nuclei. The dependence on the sample volume is simple but will be a crucial factor limiting resolution. Considering the sample volume as the size of voxel, the improving resolution from 0.1 mm to 5 μm in all three directions will reduce the signal by a factor of 8000. As we can see from the factors such as $(B_1/i)_{xy}$ and resistance of a coil, the design of a sensitive RF coil is also a very important requirement to achieve high signal-to-noise ratios.

3.2 Fundamental Limitations

As can be seen from Eq. 3-9, the signal-to-noise ratio in NMR microscopy is seriously reduced by small voxel size, which definitely can not be avoided if we want high resolution images. There are several other factors limiting the resolution. In a systematic treatment all of the limitations may be classified as either intrinsic limitations or extrinsic limitations. Intrinsic properties are related solely to the liquid itself, while extrinsic properties are also a function of the surroundings. These are summarized in table 3-1.

Since the image resolution be defined as the full-width-half-maximum (FWHM) of the point spread function of the image^[3-16], intrinsic limitations to the resolution are describable in terms of spatially uniform partial point spread functions which contribute to the broadening of the total point spread function. Then, the observable image is the convolution,

$$\text{Image} = \text{Object function} \otimes \text{PSF}_{\text{total}} + \text{Noise}, \quad [3-10]$$

where the object function is the spin density that one wants to measure, and the total point

Table 3-1. Intrinsic and extrinsic limitations on resolution

| Mechanism | Intrinsic/Extrinsic | Comments |
|--------------------------|---------------------|--|
| Spins per volume element | intrinsic | spin density of water = 7×10^{10} spins/ μm^3 |
| Sampling finite k-space | intrinsic | set by the experimenter |
| T ₂ | intrinsic | |
| Chemical shift | intrinsic | refocusable |
| Magnetic susceptibility | extrinsic | refocusable |
| Free diffusion | intrinsic | |
| Bounded diffusion | extrinsic | |

spread function is a convolution of each contributing PSF,

$$\text{PSF}_{\text{total}} = \text{PSF}_{\text{spins}} \otimes \text{PSF}_{\text{sampling}} \otimes \text{PSF}_{\text{T}_2} \otimes \text{PSF}_{\text{chemical}} \otimes \text{PSF}_{\text{diffusion}}.$$

[3-11]

The most important contribution to the point spread function at resolutions higher than 10 μm is from molecular diffusion. To create a magnetization grating for spatial encoding, linear magnetic field gradients are applied across the sample and spins at each position evolve under the gradients. The motion of spins due to molecular diffusion in the presence of the gradients blurs the grating and reduces the signal intensity. This effect becomes very important as the size of voxel is reduced, especially at resolutions beyond 10 μm where the time necessary to create a magnetization grating of a given period in the sample is of the same order as the time necessary for molecules to randomly diffuse over the grating spacing. This is the ultimate limitation to the resolution in NMR microscopy.

The line broadening by T₂ relaxation and chemical shifts is commonly avoided by using an optimal gradient strength that makes the bandwidth of each voxel match the spectral broadening. In most NMR microscopy, these are not the main limiting factors in resolution.

Two important effects, the magnetic susceptibility and bounded diffusion, are spatially non-uniform and hence are not describable as a blurring of the point spread function. The field gradient induced by inhomogeneous magnetic susceptibility in a sample, interferes with the applied gradient and degrades the linearity of the applied gradient. This introduces spatially non-uniform image distortions. As we know from

section 2-2, however, this artifact only appears along the frequency encoding direction and may be reduced by using strong gradients. The existence of boundaries within a sample restricts molecular diffusion and the signal attenuation at the boundaries is less than in the bulk regions. This bounded diffusion will introduce bright features in an image.

Chapter 4

Effects of Molecular Diffusion

It is widely accepted that the single most important factor in NMR microscopy is molecular diffusion [4-1, 2, 3, 4]. It not only broadens the point spread function but also seriously reduces the signal-to-noise ratio. In this section a general formalism for molecular diffusion is introduced and used to analyze its effects in various cases.

4.1 General Formalism

Magnetization gratings are the essence of NMR imaging and they are created by the spatially dependent phase evolution of spins under magnetic field gradients. The phase evolution of the spins is disturbed by molecular diffusion, which is random in nature and which always exists in liquid samples. In other words, molecular diffusion in the presence of magnetic field gradient induces an irreversible uncertainty in the phase of spins, and, thereby, blurs the magnetization grating and reduces the signal intensity. These effects are illustrated in Fig. 4-1. The effects becomes extremely important in NMR microscopy, especially when the time to create a magnetization grating of a given period in a sample is of the same order as the time for the molecules to randomly diffuse over the same distance.

The phase accumulated by spins due to diffusion ϕ_D in the presence of a spatially uniform magnetic field gradient, $\mathbf{G}(t)$, is given by

$$\phi_D(t) = \gamma \int_0^t \mathbf{G}(t') \cdot [\mathbf{r}(t') - \mathbf{r}(0)] dt'. \quad [4-1]$$

In the absence of diffusional barriers, ϕ_D is independent of the initial position $\mathbf{r}(0)$ while for restricted diffusion it depends on $\mathbf{r}(0)$. The expression for the signal attenuation due to diffusion may be obtained by from Torrey's equation^[2-12] or by using a random walk model^[4-5]. The calculation of the signal attenuation for restricted diffusion is very complicated and thereby, is usually simulated^[4-3,7]. However, for free diffusion it is rather simple and the diffusion dependent average square phase fluctuation is given by

$$\sigma_\phi^2(t) = 2\gamma^2 D \int_0^t \left[\int_{t'}^t G(t'') dt'' \right]^2 dt', \quad [4-2]$$

where D is the diffusion constant and $G(t)$ is the time dependent field gradient. Assuming

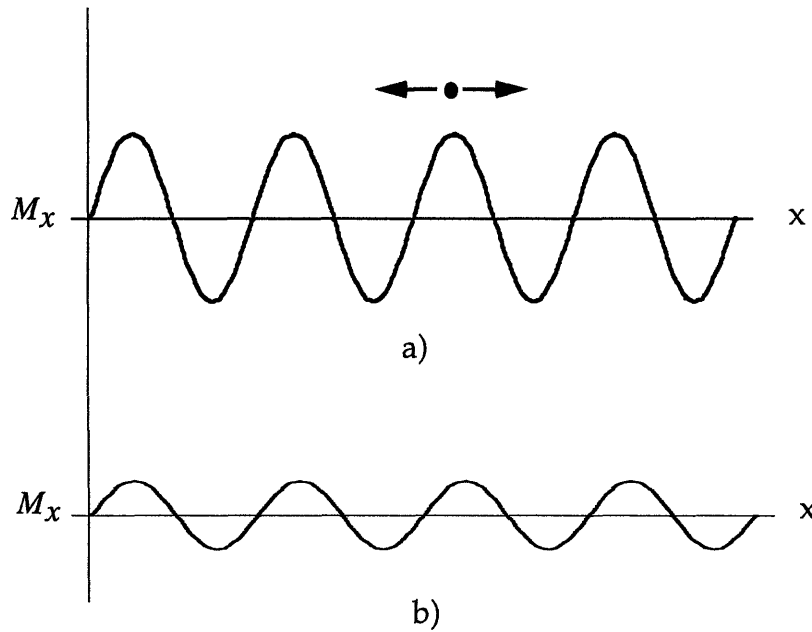


Figure 4-1. Signal attenuation due to free diffusion. (a) initial magnetization grating, (b) final magnetization grating. The intensity of grating is reduced by molecular free diffusion across the grating while the period of grating is preserved.

that the probability distribution of ϕ_D is Gaussian, then the diffusional signal attenuation factor, $A(t)$, is

$$A(t) = \exp\left(-\sigma_\phi^2(t) / 2\right). \quad [4-3]$$

By using Eq. 4-2 and 4-3, we can calculate the attenuation factor for any gradient waveform. For a constant gradient G , the attenuation factor is

$$A(t) = \exp\left(-\gamma^2 G^2 D t^3 / 3\right). \quad [4-4]$$

4.2 Diffusive Signal Attenuation and Gradient Strength

To understand the relation between the gradient strength and the diffusional signal attenuation, it is enough to consider free diffusion in the presence of a constant field gradient. As shown in Eq. 4-4, the signal attenuation factor depends on the gradient strength, the diffusion constant, and the gradient on-time. All these parameters may be controlled by experimenter. The diffusion constant may be reduced by decreasing the temperature of the sample but this may also remove proper contrast mechanisms or may damage the sample. The control of the gradient strength and the gradient on-time must be

considered together, which becomes clear when, recalling that $k = \gamma G t / 2\pi$, and by rewriting Eq. 4-4 as,

$$A(t) = \exp(-4\pi^2 k^2 D t / 3). \quad [4-5]$$

To achieve an image with a certain resolution, the area of k-space to be collected is fixed. However, the gradient on-time still can be made arbitrarily small to reduce the diffusional signal attenuation. To implement this idea, a very strong field gradient is required to maintain the same k. This is the reason why very strong gradients are a prerequisite for high resolution NMR microscopy. The signal attenuation factors as a function of gradient on time is shown in Fig. 4-2, where the k value is taken to be $0.1 \mu\text{m}^{-1}$, and a short gradient on-time corresponds to a strong gradient and vice versa.

In most cases, extremely strong gradients are not employed since a bandwidth limit to resolution is introduced as the gradient strength is increased. The frequency spread of an image scales as the gradient strength, and so the receiver bandwidth must be proportionately increased to encompass the entire image bandwidth. As shown in Eq. 3-7, the thermal noise increases as the square root of the frequency bandwidth, and so the signal-to-noise ratio decrease with the square root of the gradient strength. Therefore, the increase of gradient strength has two conflicting contributions to the signal-to-noise ratio and can be described by,

$$SNR \propto \frac{A(t)}{\sqrt{\Delta f}} \propto \frac{\exp(-4\pi^2 k^2 D t / 3)}{\sqrt{G}}. \quad [4-6]$$

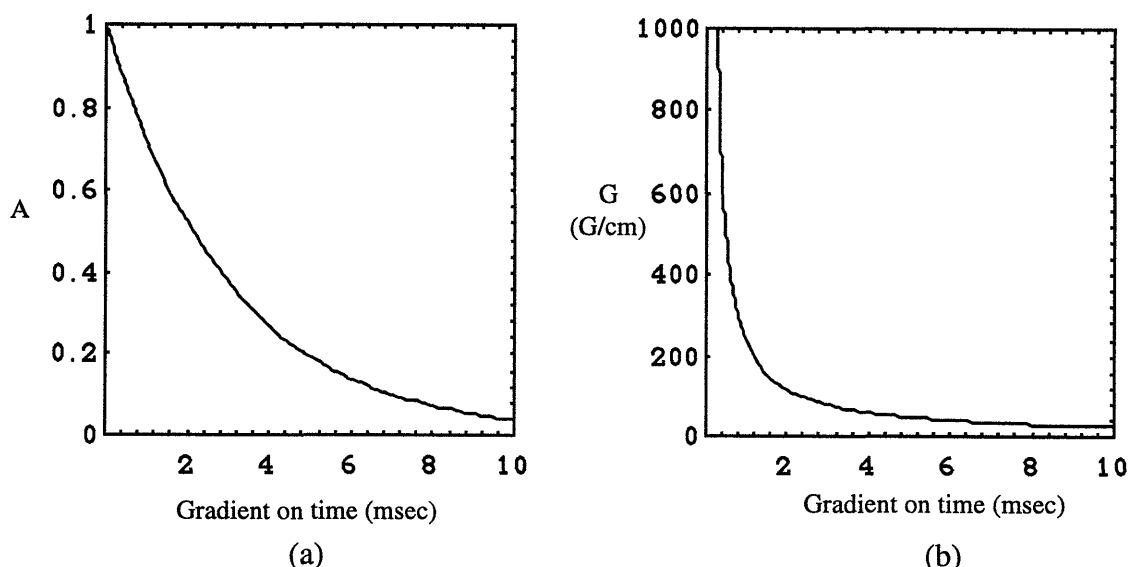


Figure 4-2. (a) Diffusional signal attenuation factor, and (b) gradient strength as a function of gradient on time. Shorter gradient on time corresponds to stronger gradient. $k = 0.1 \mu\text{m}^{-1}$ and $D = 0.25 \mu\text{m}^2/\text{msec}$.

This relation is shown schematically in Fig. 4-3, in which we can see that for very strong gradients the signal-to-noise ratio is limited by the bandwidth problem and falls off rapidly, while for weaker gradients the signal-to-noise ratio is limited by molecular diffusional signal attenuation.

The bandwidth problem can be overcome by a remarkably simple idea, turning off the gradient during data collection. It was shown in chapter 2 that there are two ways of spatial encoding, phase encoding and frequency encoding. In the phase encoding method the gradient is off during data collection while in the frequency encoding method the gradient is on. If we employ phase encoding in all three directions, our experiments become free of the bandwidth problem associated with the strong gradient, and the signal-to-noise ratio monotonically increases with the gradient strength. In this case the detection bandwidth is not the bandwidth of the image but the bandwidth of the NMR spectrum, which is orders of magnitude smaller. The NMR spectrum bandwidth is about 1 kHz while the image bandwidth is about 400 kHz when a gradient strength 1000 G/cm is used for a 1 mm sample.

The imaging method which uses phase encoding in all three direction is called 'constant time imaging'. This method will be thoroughly discussed and analyzed in the chapter 5.

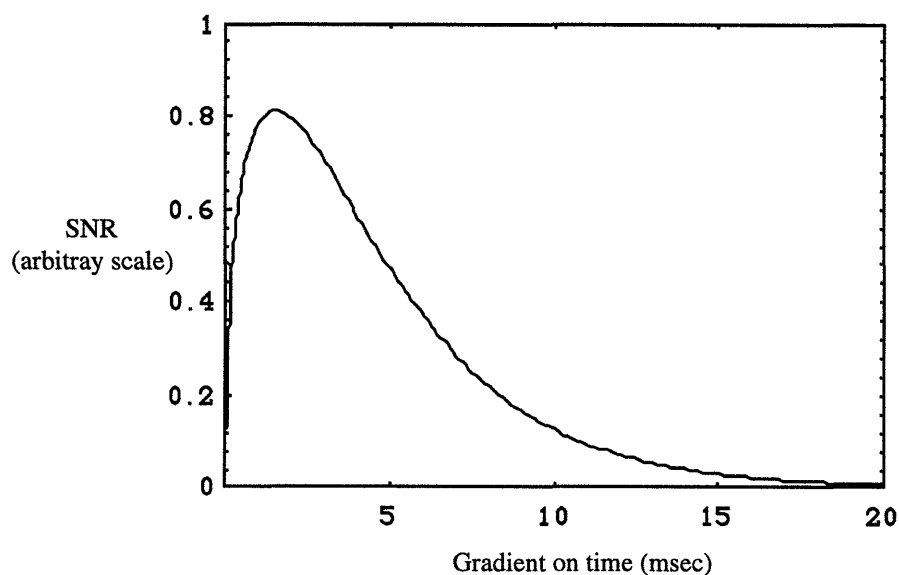


Figure 4-3. Signal-to-noise ratio as a function of gradient on-time for the case that gradient is left on during data collection. Shorter gradient on-time corresponds to stronger gradient. $k = 0.1 \mu\text{m}^{-1}$ and $D = 2.5 \mu\text{m}^2/\text{msec}$

4.3 Diffusive Signal Attenuation in Frequency Encoding and Phase encoding

The diffusive signal attenuations for frequency encoding and phase encoding are analyzed for various resolutions and gradient strengths. This is important to understand the proper approaches to overcoming the diffusion effects in NMR microscopy.

A typical frequency encoding sequence is shown in Fig. 4-4, in which a spin echo is employed and the data are collected during the second gradient pulse, called a readout gradient. The diffusional signal attenuation factor for this sequence is obtained from Eq. 4-2 and 4-3,

$$A(t) = \exp(-\gamma^2 D(\Gamma_1 + \Gamma_2 + \Gamma_3)), \quad \text{for } T_a + T_b < t < T_a + T_b + T_{acq}, \quad [4-7]$$

where,

$$\Gamma_1 = \frac{1}{3G_1} \left([G_2(t - T_a - T_b)]^3 + [G_1 T_a - G_2(t - T_a - T_b)]^3 \right),$$

$$\Gamma_2 = G_2^2 (t - T_a - T_b)^2 T_b,$$

$$\Gamma_3 = \frac{G_2^2}{3} (t - T_a - T_b)^3.$$

The gradient strength and its duration are determined by the maximum k value for the desired image resolution. From the Nyquist condition, the maximum k-value k_{\max} to

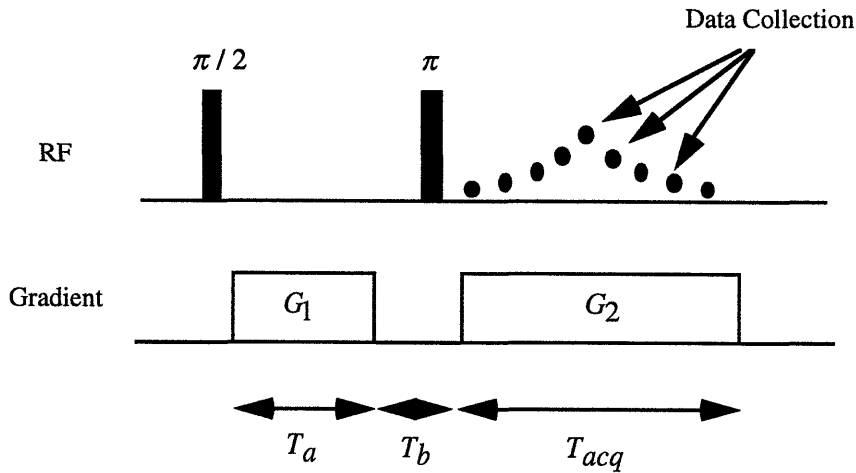


Figure 4-4. Pulse sequences for frequency encoding.

achieve a k-space limited resolution Δx_k is,

$$k_{\max} = \frac{1}{2\Delta x_k}. \quad [4-8]$$

The maximum k value, k_{\max} , is related to G_1 , G_2 , and their durations by,

$$k_{\max} = \frac{1}{2\pi} \gamma G_2 (T_{acq}/2) \quad [4-9]$$

$$G_1 T_a = G_2 T_{acq}/2.$$

The second equation in Eq. 4-9 makes the center of the acquisition period correspond to the center of k-space. In this analysis, the value of G_2 was determined by the optimal condition in which the frequency width of each pixel is equal to the spectral width of the sample,

$$SW_{\text{sample}} = \frac{1}{2\pi} \gamma G_2 \Delta x_k. \quad [4-10]$$

As shown in section 2.3 the spin echo sequence refocuses all time independent internal Hamiltonians and the magnetic susceptibility effects at the echo center. In most very small samples as is the case for NMR microscopy, the magnetic susceptibility variation across the sample is large and so for sensitivity reasons spin echo sequences are preferred to gradient echo sequences. To assure this, the spin echo center must be located at the center of the acquisition period which corresponds to the center of k-space, $k=0$. Therefore, the time durations satisfy the following relation,

$$T_a + T_b = T_{acq} / 2. \quad [4-11]$$

This relation provide another constraints on the parameters to be set.

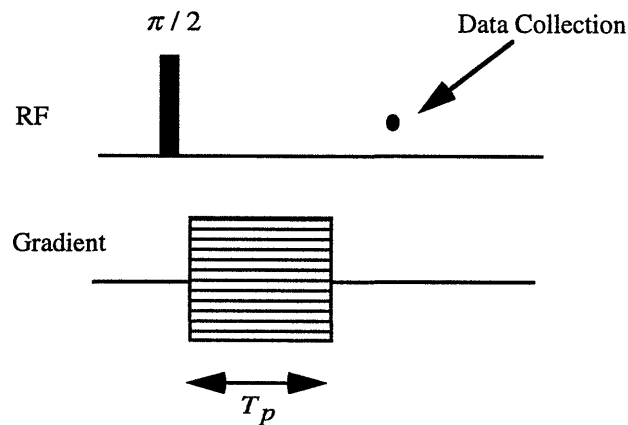


Figure 4-5. Pulse sequence for constant time phase encoding

A typical pulse sequence for phase encoding is shown in Fig. 4-5. The diffusional signal attenuation factor for this sequence is very simple,

$$A(T_p) = \exp(-\gamma^2 G^2 D T_p^3 / 3). \quad [4-12]$$

The maximum gradient strength and the gradient on-time, called the phase encoding time, are determined by,

$$k_{\max} = \frac{1}{2\pi} \gamma G_{\max} T_p. \quad [4-13]$$

The diffusional signal attenuations and corresponding point spread functions in frequency encoding and phase encoding are calculated and compared with each other at resolutions, 20, 10, 5, and 3 μm . In this calculation, the diffusion constant is assumed to be 2.5 $\mu\text{m}^2/\text{msec}$ (that of free water) and the spectral bandwidth of sample is 1 kHz. Other parameters used are given in table 4-1. G_1 during frequency encoding and G_{\max} during phase encoding are not limited by the bandwidth problem and are taken to be 1000 G/cm, the maximum gradient strength of the NMR microscope developed here.

The results given in Fig. 4-6,7,8, and 9, show that the signal attenuation in the phase encoding is always smaller than in the frequency encoding, this becomes very pronounced as the resolution increases.

In frequency encoding, the signal attenuation is small at 20 μm resolution, but becomes appreciable at 10 μm and severe at 5 μm and 3 μm , and so does the blurring of point spread function. This means that when frequency encoding is used, the molecular diffusion effect becomes a very important factor in the resolution beyond 10 μm . The blurring of the point spread function comes from the k-dependent signal attenuation. The envelope of the signal attenuation is asymmetric about the

Table 4-1. The gradient strength and the gradient on-times used in the calculation of the diffusive signal attenuation factors.

| Δx_k (μm) | Frequency encoding | | | | | Phase encoding | |
|-----------------------------------|--------------------|-----------------|-----------------|-----------------|----------------------------|----------------------|-----------------|
| | G_1 (G/cm) | G_2 (G/cm) | T_a (msec) | T_b (msec) | T_{acq} (msec) | G_{\max} (G/cm) | T_p (msec) |
| 20 | 1000 | 117 | 0.06 | 0.44 | 1.0 | 1000 | 0.059 |
| 10 | 1000 | 235 | 0.12 | 0.38 | 1.0 | 1000 | 0.117 |
| 5 | 1000 | 470 | 0.23 | 0.27 | 1.0 | 1000 | 0.234 |
| 3 | 1000 | 783 | 0.39 | 0.11 | 1.0 | 1000 | 0.390 |

echo center at $k=0$ and the peak of the envelope is shifted left. This comes from the effective fast refocusing effect^[4-5] at the beginning of the readout gradient, G_2 . Another important point to be noticed is that the signal at the center of the k-space, $k=0$, is attenuated, which leads to an overall loss in the image signal-to-noise ratio.

In phase encoding, the signal attenuation is negligible at 20, 10, and 5 μm resolution. At 3 μm resolution there is some attenuation at high k-space but it is still small. The blurring of the point spread function is negligible in all cases. This means that if we use phase encoding with 1000 G/cm gradient strength, molecular diffusion is not a limiting factor in the resolution up to 3 μm . In fact, 1000 G/cm gradient strength may be used even at 2 μm resolution. What must be noticed in phase encoding is that the envelope of the signal attenuation is symmetric about the echo center, $k=0$, where the signal attenuation is always zero. This means that there may be a blurring of the image when weaker gradients are used, but the overall image signal-to-noise ratio will not be effected by molecular diffusion^[4,9].

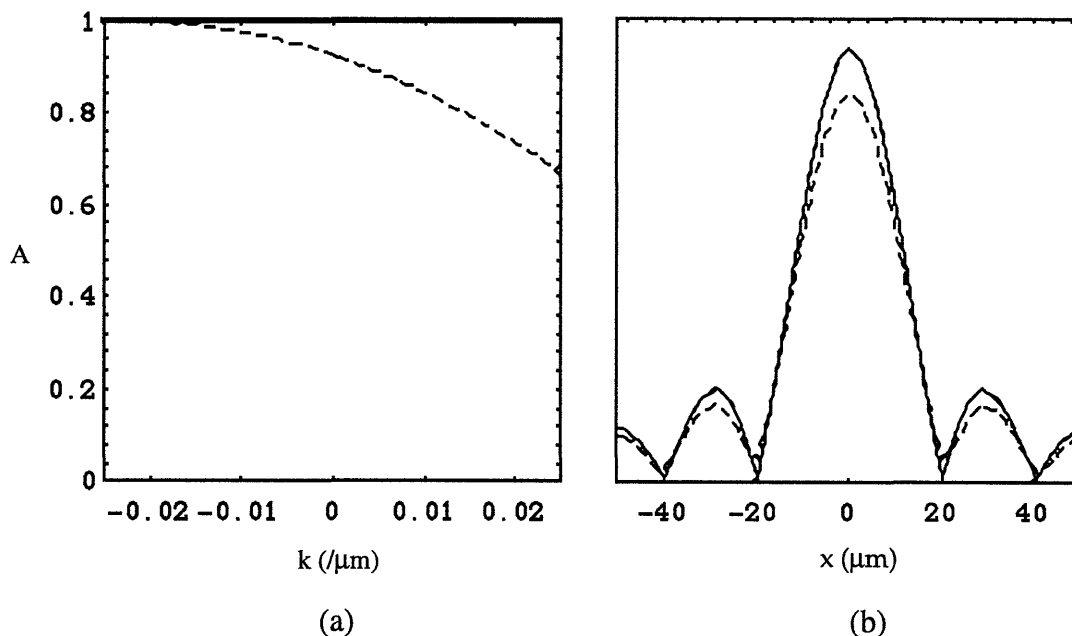


Figure 4-6. The diffusional signal attenuation factors and the point spread functions for 20 μm resolution. (a) the signal attenuation factor, and (b) the point spread function. The solid line is for phase encoding and the dashed line is for frequency encoding. The thin dashed line in the point spread function is for the case of no diffusion, which is overlapped with the solid line.

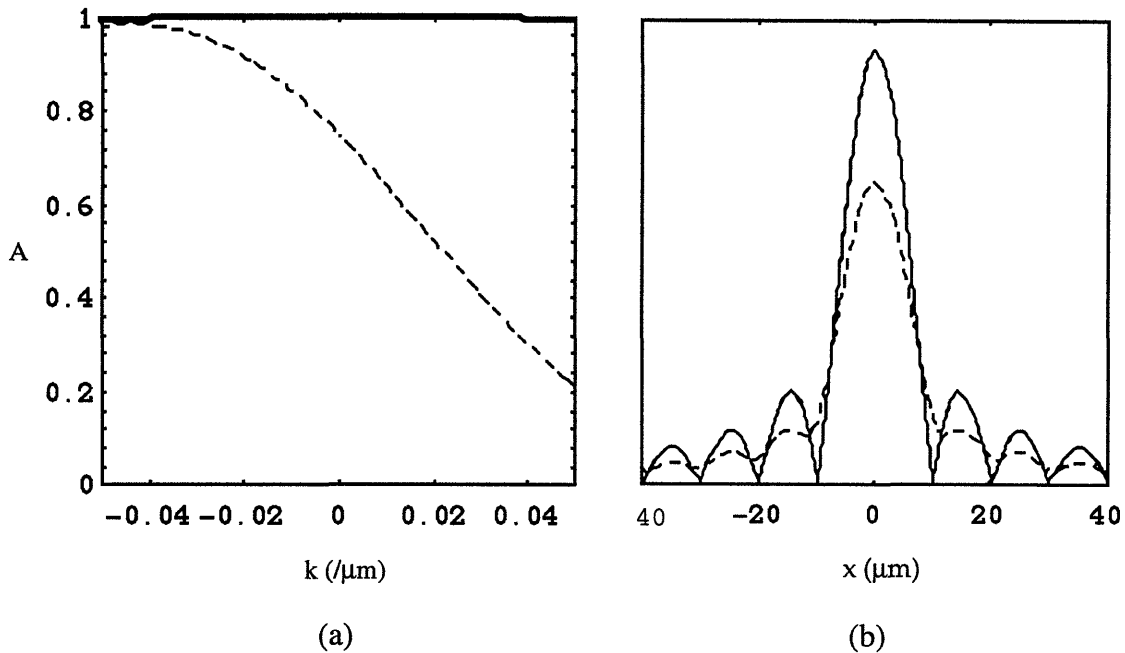


Figure 4-7. The diffusional signal attenuation factors and the point spread functions for 10 μm resolution. (a) the signal attenuation factor, and (b) the point spread function. The solid line is for phase encoding and the dashed line is for frequency encoding. The thin dashed line in the point spread function is for the case of no diffusion, which is overlapped with the solid line.

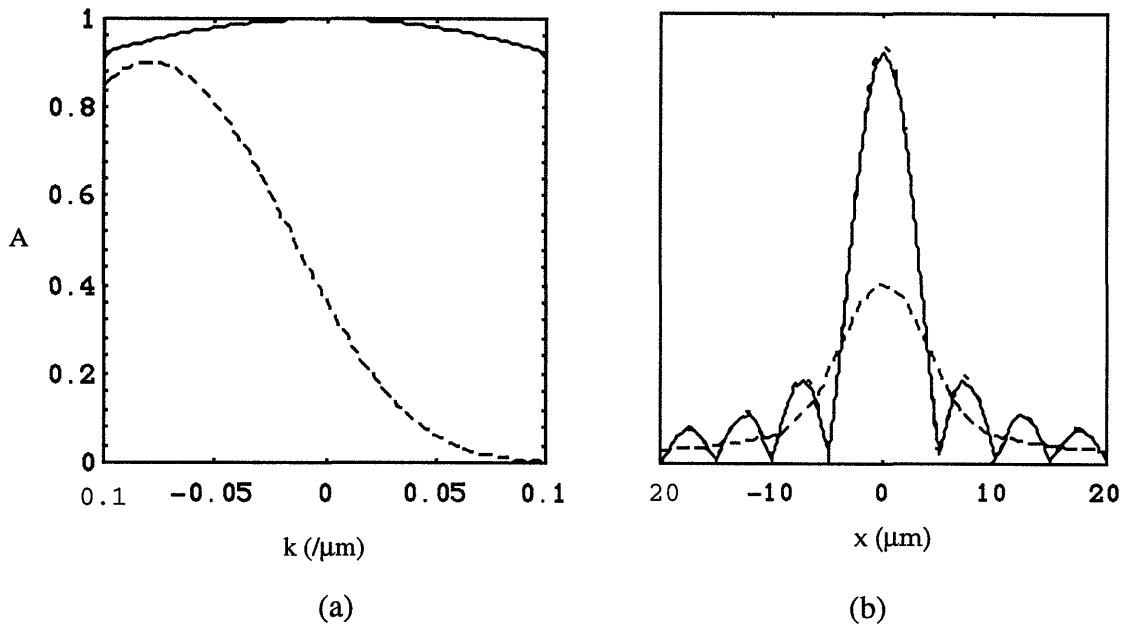


Figure 4-8. The diffusional signal attenuation factors and the point spread functions for 5 μm resolution. (a) the signal attenuation factor, and (b) the point spread function. The solid line is for phase encoding and the dashed line is for frequency encoding. The thin dashed line in the point spread function is for the case of no diffusion.

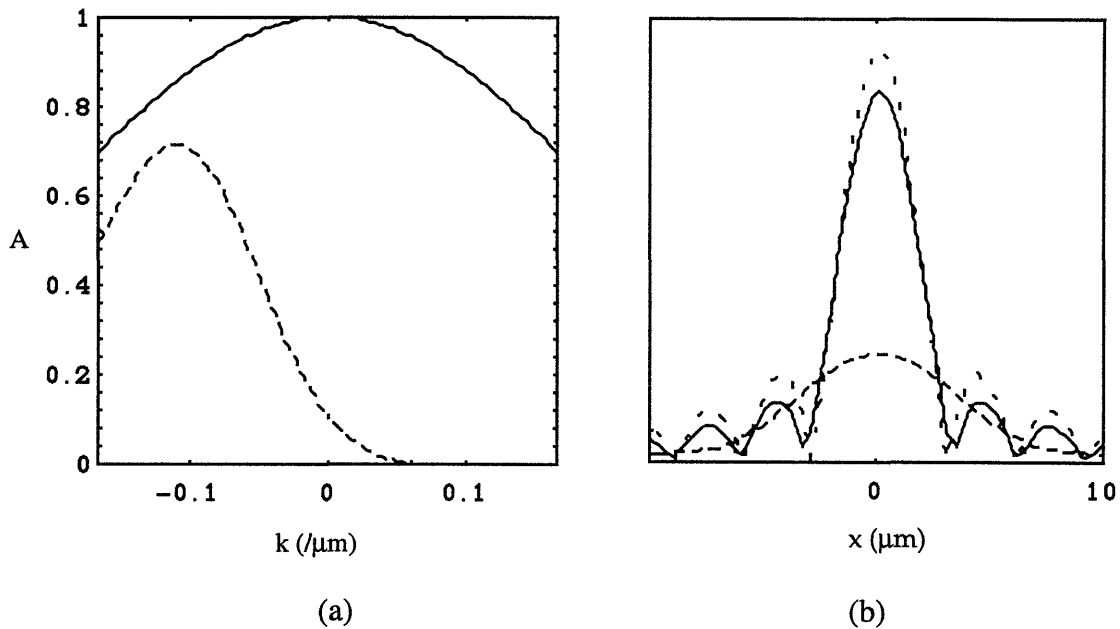


Figure 4-9. The diffusional signal attenuation factors and the point spread functions for $3 \mu\text{m}$ resolution. (a) the signal attenuation factor, and (b) the point spread function. The solid line is for phase encoding and the dashed line is for frequency encoding. The thin dashed line in the point spread function is for the case of no diffusion.

There is an alternative method of phase encoding in which the gradient strength is kept constant and the gradient on-time is changed in step. This sequence, shown in Fig. 4-10, enables us to use the maximum gradient strength over all k -space and therefore this may lead to a further reduction of the diffusional signal attenuation. In Fig. 4-11, two phase encoding methods are compared with each for two resolutions, $5 \mu\text{m}$ and $2 \mu\text{m}$. Since the signal attenuation factor is symmetric about $k=0$, only half the k -space is shown. In both cases, the maximum gradient strength was 1000 G/cm . At $5 \mu\text{m}$ resolution, the difference is hardly noticed but at $2 \mu\text{m}$, the time-varying phase encoding shows less signal attenuation than the constant time phase encoding except at $k=0$ and $k=k_{\text{max}}$. Considering the whole k -space, the difference at $2 \mu\text{m}$ resolution is about 10%. This difference may be more pronounced if the resolution becomes even higher. In that case, however, the overall signal attenuation will be severe in both methods and so will the blurring of the point spread function. Therefore, the time-varying phase encoding provides a modest improvement over the constant time method.

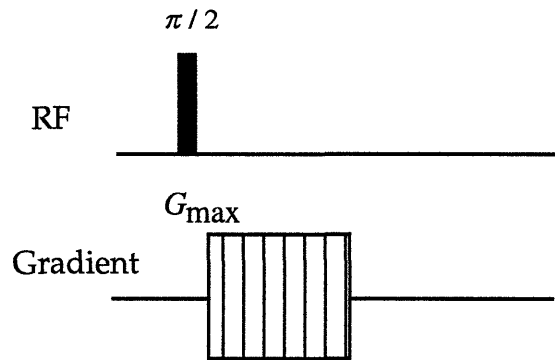


Figure 4-10. A pulse sequence for time-varying phase encoding

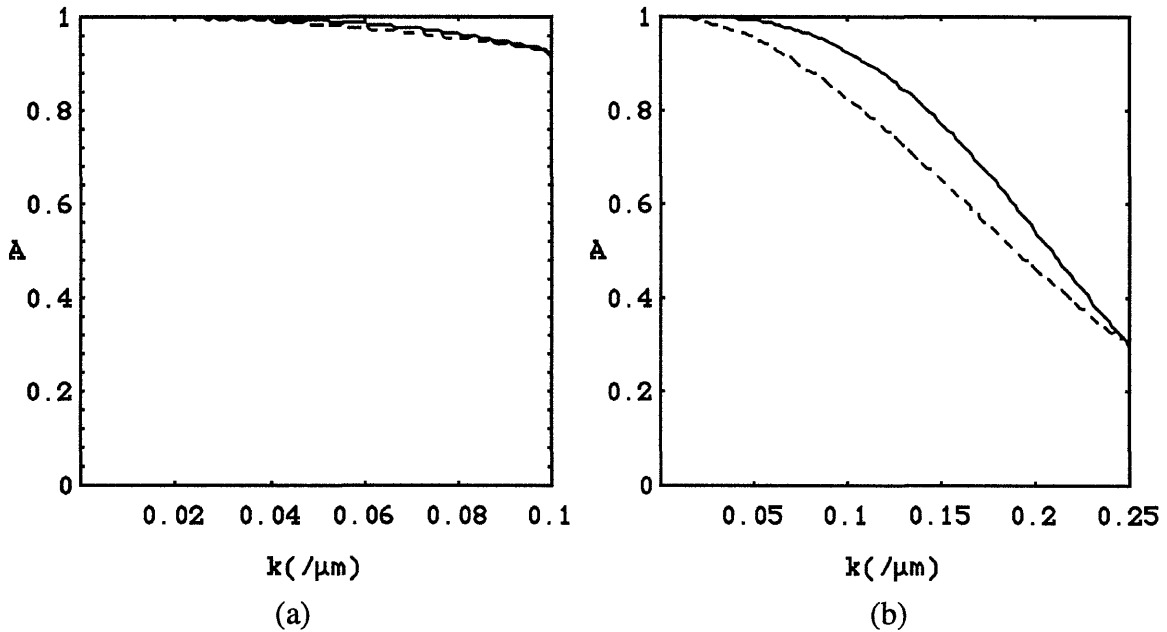


Figure 4-11. Signal attenuation factors for time-varying phase encoding and constant time phase encoding. (a) $5 \mu\text{m}$ and (b) $2 \mu\text{m}$ k-space limited resolution. The solid line is for time-varying phase encoding and the dashed line for constant time phase encoding.

4.5 Diffusive Signal Attenuation during Slice Selection

In a slice selection process, a gradient is applied while a soft RF pulse is on. This means that there will be signal attenuation due to molecular diffusion during this process. In most cases, this effects has not been an important issue because the thickness of the slice is out of the region where the molecular diffusion becomes effective. It has been general trend that in 2D imaging, to improve in plane resolution the slice thickness was made rather large. This trend is simply because, in most cases, the available signal-to-noise ratio is not sufficient to achieve a thin slice while keeping the inplane resolution high. However, if there is a margin in signal-to-noise ratio to adopt a thin slice with high inplane resolution, the issue of signal attenuation during slice selection becomes important. Of course, for 3D imaging the slice thickness is not necessarily small. However, 3D imaging is not always an efficient way of taking images for every experiemnt. In this section, the estimation of this effect is presented and a presaturation slice selection, as a possible solution, is suggested.

A typical slice selection sequence is shown in Fig. 4-12, in which the first gradient and the refocusing gradient are assumed to have the same amplitude and opposite sign. The diffusional signal attenuation factor for this sequence may be calculated directly from Torrey's equation. For simplicity, however, it was obtained by the following argument.

If molecular diffusion is ignored, the transverse magnetization in a selected slice are in phase at the end of the refocusing gradient. For this to be correct, the transverse

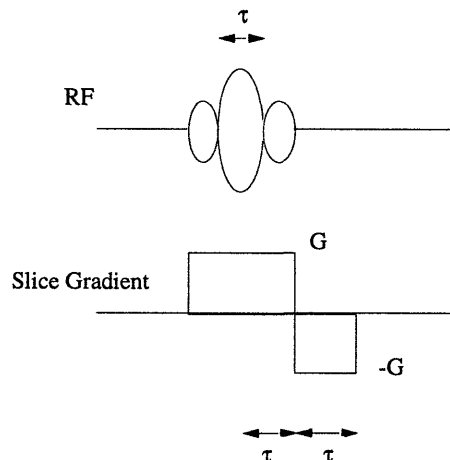


Figure 4-12. A pulse sequence for slice selection.

magnetization just before the refocusing gradient should have a phase, $\exp(i\gamma G x \tau)$ which is made by the soft pulse and the first gradient. Concerning only of the phase of the transverse magnetization in the slice, this phase could be made by a hard pulse followed by a gradient G for τ . Of course, by doing this we would not select a slice. However, since we are concerned only with the signal attenuation effect during the slice selection, this approximation to obtain the signal attenuation factor is reasonable. Based on this assumption, the signal attenuation accumulated during slice selection is,

$$A(\tau) = \exp(-2\gamma^2 G^2 D \tau^3 / 3). \quad [4-13]$$

The gradient strength, G , and the gradient on time, τ , are determined by the slice thickness and the shape of the soft pulse. If a 2 cycle sinc function is used for the soft pulse and the pulse duration is 2τ , the excitation bandwidth, Δf_{excite} , is $2/M_x$. This excitation bandwidth is related to the slice thickness, Δx_{excite} , as,

$$\Delta f_{excite} = \frac{1}{2\pi} \gamma G \Delta x_{excite}. \quad [4-14]$$

For a given τ , the gradient strength required is,

$$G = \frac{4\pi}{\gamma \tau \Delta x_{excite}}. \quad [4-15]$$

Then the signal attenuation factor can be expressed in terms of Δx_{excite} ,

$$A(\tau) = \exp\left(-\frac{32D\tau}{3\pi^2 \Delta x_{excite}^2}\right). \quad [4-16]$$

The signal attenuation factor and the required gradient strength as a function of slice thickness are shown in Fig. 4-13 and 4-14.

In Fig. 4-13 the excitation bandwidth was set at 1 kHz, a common spectral bandwidth for an NMR microscopy sample. The signal loss is about 5 % even at 100 μm and rapidly increases as the slice becomes thinner. At 20 μm it is as much as 73 %. However if the excitation bandwidth is increased by using a shorter cycle time and a stronger slice gradient, the signal loss will be reduced. When the excitation bandwidth is set at 4 kHz, as shown in Fig. 4-14, the signal loss is less than 5 % at 50 μm , and is 28 % at 20 μm . The gradient strength for 50 μm slice is 188 G/cm, and, for 20 μm , is 470 G/cm. This tells us that with slices as thin as 50 μm the signal loss can be restricted by using a reasonably high gradient, but the conventional slice selection method may be unsuitable for thinner slice due to diffusive signal attenuation.

An alternative method of slice selection is to presaturate the magnetization outside of the slice to be selected. This has been used in volume selective NMR spectroscopy^[4-10].

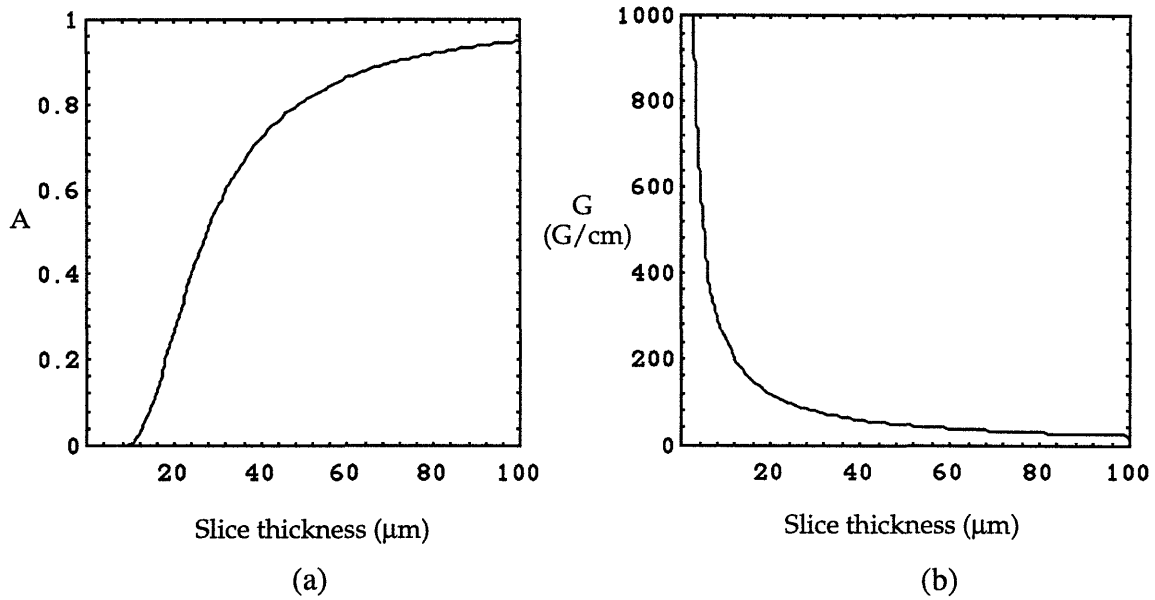


Figure 4-13. a) Diffusive signal attenuation factor and b) slice gradient strength as a function of slice thickness. $\Delta f_{excite} = 1$ kHz ($\tau = 2.0$ msec) and $D = 2.5 \mu\text{m}^2/\text{msec}$ (free water)

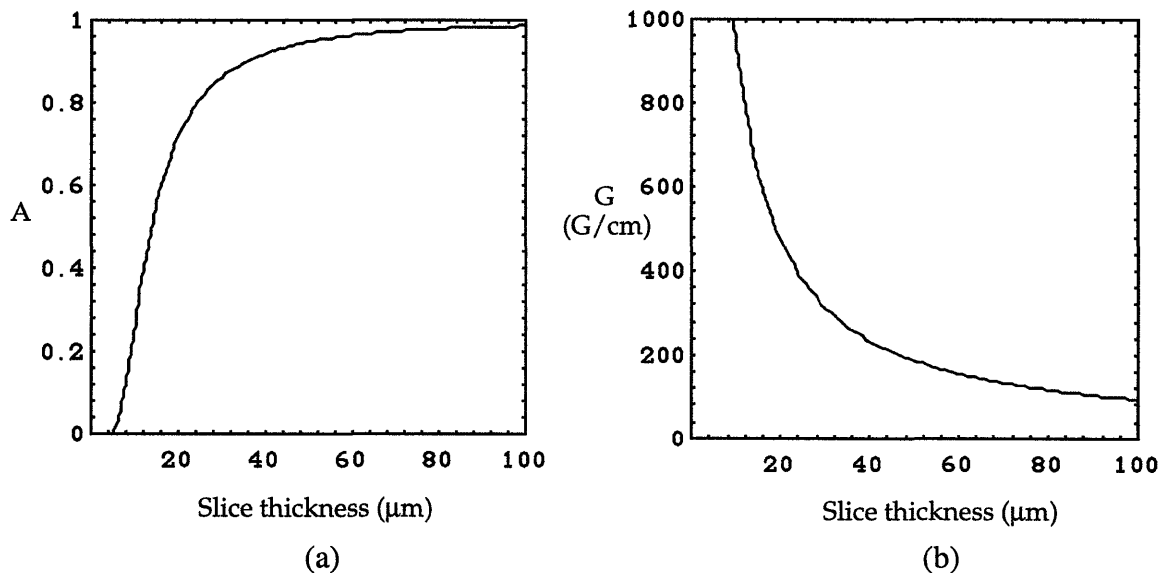


Figure 4-14. (a) Diffusive signal attenuation factor and (b) slice gradient strength as a function of slice thickness. $\Delta f_{excite} = 4$ kHz ($\tau = 0.5$ msec) and $D = 2.5 \mu\text{m}^2/\text{msec}$.

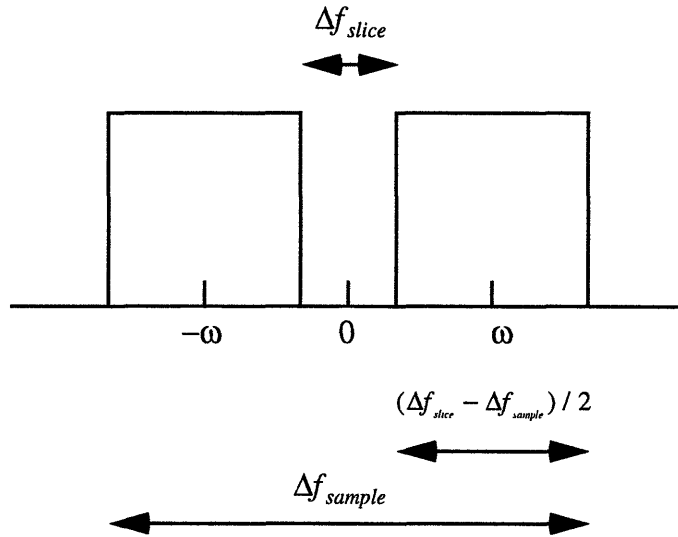


Figure. 4-15. Frequency profile for presaturation slice selection

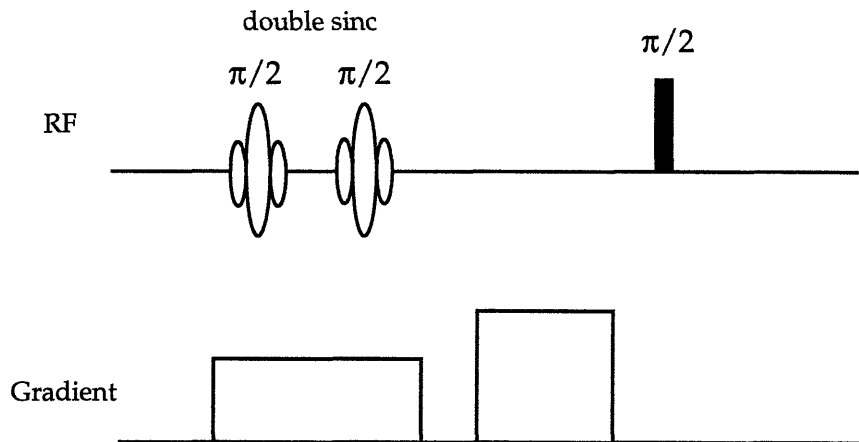


Figure 4-16. Pulse sequence for presaturation slice selection. The double sinc pulse in the presence of gradient excites spins outside of a specific layer and the second gradient dephase the transverse magnetization. Then a hard $\pi/2$ pulse is applied to excite the spins within the slice.

The frequency profile required, shown in Fig. 4-15, is the reverse of that required in the conventional slice selection. This profile can be achieved by using a cosine modulated sinc function or a double sinc function.

As shown in Fig. 4-16, the magnetization outside the slice is excited by applying the shaped RF pulse while a gradient along the slice direction is on. The excited magnetization will be totally dephased by the crushing gradient that follows. After this, a

hard pulse is applied without any gradient to excite the magnetization in the slice. This method preserves the magnetization in the slice.

The quality of presaturation will be affected by the longitudinal relaxation recovery of the saturated spins and the homogeneity of the RF coil. Another limitation of this method is that it can not be used to acquire a 3D image, because an additional gradient for spatial encoding along the slice direction, may effectively refocus the dephasing of the magnetization outside the slice. We may avoid this problem by applying a very high crushing gradient for a long time and strongly attenuate the signal by diffusion so that no refocusing is possible. However, this would induce a gradient heating problem and permits signal recovery due to T_1 relaxation before the hard pulse.

Chapter 5

Constant Time Imaging

As demonstrated in the previous chapters, phase encoding is much more effective at restricting the signal attenuation due to molecular diffusion than frequency encoding. Therefore, constant time imaging (CTI) which uses only phase encoding in all spatial encoding will be very effective in reducing diffusion effects. In this chapter, the general features of CTI and the analysis of its sensitivity are presented. For further improvement of the signal-to-noise ratio, a CPMG sequence is suggested in combination with CTI.

5.1 General Description

Constant time imaging (CTI), shown in Fig. 5-1, uses only phase encoding in all spatial encoding^[5-1,2] and collects a single data point at a fixed evolution time. Magnetization grating for each data point are generated during a gradient evolution period and in subsequent acquisitions the gradient strength is incrementally changed. The evolution of spins due to time independent Hamiltonians, such as the secular component of the chemical shift, magnetic susceptibility, and dipolar coupling will be constant and unobserved. However, since the Hamiltonian for gradient interaction changes from data point to data point the spin evolution due to gradient will be observed and so an area of k-space sufficient to reconstruct an image can be acquired. Therefore, an image by constant time imaging is free from artifacts induced by time independent internal Hamiltonians, and magnetic susceptibility. This method has been employed in solid state imaging where the wide line induced by internal Hamiltonian is problematic^[5-2]. In liquid state imaging, CTI will also be very effective in restricting the signal attenuation due to molecular diffusion since it uses only phase encoding in all spatial encoding. The effectiveness of phase encoding with strong gradient is well demonstrated in chapter 4. Unfortunately it has the drawback that since only a single data point in k-space is collected per excitation, it takes a long time to acquire the required area of k-space to reconstruct an image. For example, in CTI, an 3D image of $N \times N \times N$ voxels takes an experiment time of $N^3 \times T_R$, while in spin echo imaging (SEI) it takes only $N^2 \times T_R$. In the following section, the sensitivity of CTI is compared with that of SEI.

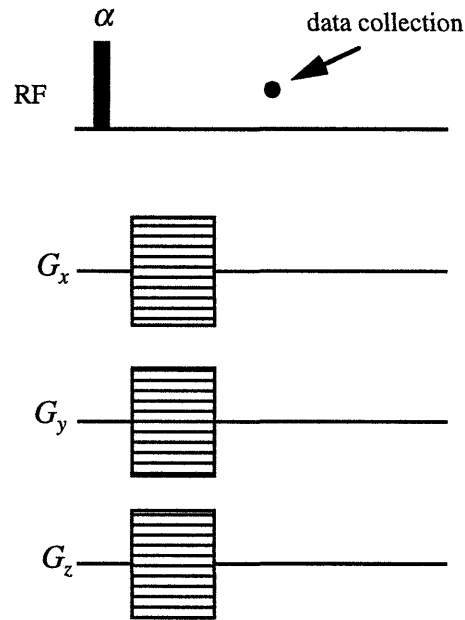


Figure 5-1. Constant time imaging. In all directions phase encoding is used.

5.2 Sensitivity of Constant Time Imaging

Before we perform a rigorous analysis on the sensitivity, it is helpful to consider a simple argument on the sensitivity of CTI and SEI. In NMR microscopy, the three main factors contributing to the signal-to-noise ratio of an image are the molecular diffusion, the detection bandwidth, and the total experiment time.

Considering only the detection bandwidth for an image of $N \times N \times N$ voxel, the signal-to-noise ratio obtainable in a single signal averaging can be expressed as follows,

$$SNR_{CTI} = C \frac{S_T}{\sqrt{\Delta f_{spect}}},$$

$$SNR_{SEI} = C \frac{S_T}{\sqrt{N \Delta f_{spect}}},$$
[5-1]

where C is a constant and S_T is a total signal detected. As mentioned in section 4-2, the detection bandwidth in CTI is the bandwidth of the NMR spectrum of the sample while in SEI it is the bandwidth of image. Assuming that an optimal bandwidth is used in SEI, then the detection bandwidth of SEI is N times larger than that of CTI and so the signal-to-noise ratio of the image by SEI is less than that of CTI by a factor of $1/\sqrt{N}$. However, SEI requires less experiment time by a factor of N to collect a single scan than does CTI.

Therefore, if we allow the same experiment time, $N^3 \times T_R$, we can take N signal averagings in SEI while only one averaging in CTI. This will improve the signal-to-noise ratio of SEI by a factor of \sqrt{N} . Therefore, considering only the detection bandwidth problem while keeping the experiment time same, and assuming an optimal gradient strength for SEI, the signal-to-noise ratios of both methods are same.

If the effects of molecular diffusion are included, then the signal-to-noise ratio available in a experiment time $N^3 \times T_R$ is higher in CTI than in SEI because CTI uses phase encoding in all spatial directions while SEI uses a frequency encoding in the readout direction. This is demonstrated below.

In NMR experiment, the sensitivity is usually defined as signal-to-noise ratio per unit time and can be given as,

$$SNR = \frac{S_T}{N_T \sqrt{T_T}} , \quad [5-1]$$

where S_T is the total signal intensity from n_o data points, N_T is the total r.m.s. noise intensity from n_o data points, and T_T is the total duration of data acquisition divided by T_1 . This was calculated by following the procedure adopted by J. Link and Seeling^[5-3] and S. Gravina and D.G. Cory^[5-2].

The r.m.s. noise in NMR microscopy experiment is given in Eq. 3-7. For a given NMR probe and temperature, the noise depends only on the bandwidth. Therefore the

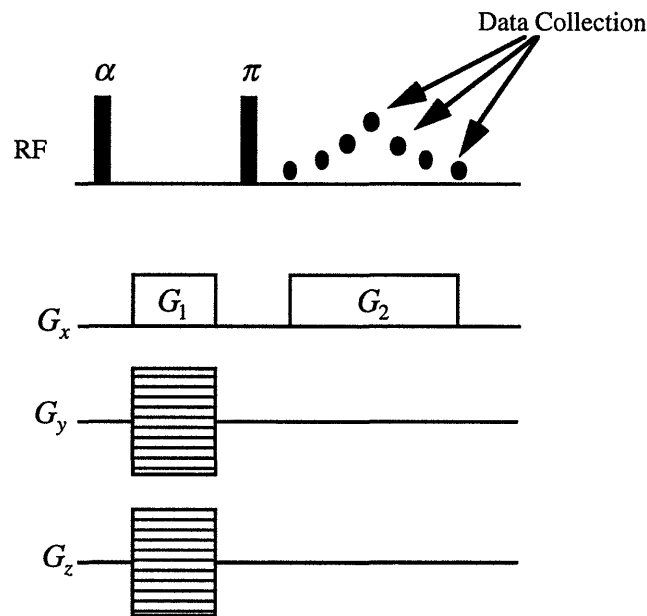


Figure 5-2. Pulse Sequence of 3D spin-echo imaging

noise can be given as,

$$N = C\sqrt{\Delta f}, \quad [5-2]$$

where C is a constant independent of the measurement technique. To compare different imaging experiment, a reference noise is defined as,

$$N_o = C \sqrt{\frac{n_o}{T_2^*}}, \quad [5-3]$$

and the noise in each data point is calculated relative to this reference noise,

$$N = N_o \sqrt{\frac{T_2^* \Delta f}{n_o}} \quad [5-4]$$

Then the total noise during acquisition of n_o data points is

$$N_T = n_o N = N_o \sqrt{n_o T_2^* \Delta f}. \quad [5-5]$$

In constant time imaging experiments, the signal measured at each step can be described in terms of four parts,

$$S(n) = S_o \exp\left(-\frac{T_p}{T_2^*}\right) G(T_R / T_1, \alpha) A(n, T_p), \quad [5-6]$$

where S_o is the signal measured immediately following a 90 degree pulse, $\exp(-T_p/T_2^*)$ is the signal loss due to relaxation during phase encoding, $G(T_R / T_1, \alpha)$ is the signal attenuation from Ernst angle excitation pulse α , and $A(n, T_p)$ is the diffusional signal attenuation factor. The Ernst angle factor^[5-2,4] is,

$$G(T_R / T_1, \alpha) = \frac{1 - E_1 \sin \alpha}{1 - E_1^2}, \quad [5-7]$$

where

$$E_1 = \cos \alpha = \exp(-T_R / T_1).$$

The steady state signal-to-noise factor ($G(T_R / T_1, \alpha) / \sqrt{T_R / T_1}$) describes the influence of the repetition time and excitation angle and has the maximum value about 0.7 when $T_R / T_1 < 0.7$. The diffusive signal attenuation factor is,

$$A(n, T_p) = A_x(n, T_p) A_y(n, T_p) A_z(n, T_p), \quad [5-8]$$

where

$$A_i(n, T_p) = \exp(-\gamma^2 G_{i,n}^2 D T_p^3 / 3) \quad , \quad i = x, y, z.$$

Then the total signal from n_o data points is,

$$\begin{aligned} S_T &= \sum_{n=1}^{n_o} S_n \\ &= S_o \exp\left(-T_p / T_2^*\right) G(T_R / T_1, \alpha) \sum_{n=1}^{n_o} \prod_{i=x,y,z} A_i(n, T_p). \end{aligned} \quad [5-9]$$

Considering that, in CTI, only one data point in k-space is detected from each excitation, the total duration of acquisition divided by T_1 is

$$T_T = \frac{n_o T_R}{T_1}. \quad [5-10]$$

From Eq. 5-5, 5-9, and 5-10, the sensitivity of CTI is,

$$SNR_{CTI} = \frac{1}{N_o n_o \sqrt{T_2^* T_R \Delta f / T_1}} S_o \exp(-T_p / T_2^*) G(T_R / T_1, \alpha) \sum_{n=1}^{n_o} \prod_{i=x,y,z} A_i(n, T_p) \quad [5-11]$$

In spin echo imaging, the detection bandwidth is n_o / T_{acq} and therefore the total noise for a single echo is,

$$N_T = N_o n_o \sqrt{\frac{T_2^*}{T_{acq}}}. \quad [5-12]$$

The signal during the acquisition time is,

$$S(t_n) = S_o \exp(-t_n / T_2) \exp(-|t_n - T_E| / T_2^*) G(T_R / T_1, T_E) A(t_n), \quad [5-13]$$

where,

$$t_n = T_p + \frac{(n-1)}{(n_o-1)} T_{acq},$$

and

$$G(T_R / T_1, T_E) = 1 - 2 \exp\left(\frac{-T_R + T_E / 2}{T_1}\right) + \exp(-T_R / T_1).$$

The steady state SNR factor $G(T_R / T_1, T_E) / \sqrt{T_R / T_1}$ has the maximum value 0.62 when $T_R = 1.5 T_1$. The diffusional signal attenuation factor in phase encoding directions are the same as in CTI and that in the readout direction is the same as was given in Eq. 4-7.

Assuming equal strengths for the first and the second gradient in the readout direction, $T_E = T_{acq} = 2T_p$ and then the total signal from a single echo is

$$S_T = \sum_{n=1}^{n_o} S_o \exp\left(-\frac{(n_o + 2n - 3)T_p}{(n_o - 1)T_2}\right) \exp\left(-\frac{|-n_o + 2n - 1|T_p}{(n_o - 1)T_2^*}\right) G(T_R / T_1, T_E) A(t_n), \quad [5-14]$$

where,

$$A(t_n) = \exp\left(-\frac{1}{3} \gamma^2 D G_x^2 \left\{ 2 \left[\frac{2(n-1)T_p}{(n_o-1)} \right]^3 - \left[\frac{(-n_o + 2n - 1)T_p}{(n_o-1)} \right]^3 \right\}\right) A_y(t_n) A_z(t_n).$$

The total duration of acquisition of a single echo divided by T_1 is

$$T_T = \frac{T_R}{T_1}. \quad [5-15]$$

From Eq. 5-12, 5-14, and 5-15, the sensitivity of SEI is,

$$SNR_{SEI} = \frac{S_o}{N_o n_o \sqrt{T_R T_2^* / T_{acq} T_1}} G(T_R / T_1, T_p)$$

$$\times \sum_{n=1}^{n_o} \exp\left(-\frac{(n_o + 2n - 3)T_p}{(n_o - 1)T_2}\right) \exp\left(-\frac{|-n_o + 2n - 1|T_p}{(n_o - 1)T_2^*}\right) A(t_n). \quad [5-16]$$

When we consider the diffusion effects, as a "rule of thumb" the parameter of significance is $\Delta x_{diff} / \Delta x_{pixel}$, where Δx_{diff} is the one dimensional r.m.s displacement of spins over a gradient on-time and Δx_{pixel} is a pixel resolution of an image. Δx_{diff} , Δx_{pixel} , and $\Delta x_{diff} / \Delta x_{pixel}$ are given below,

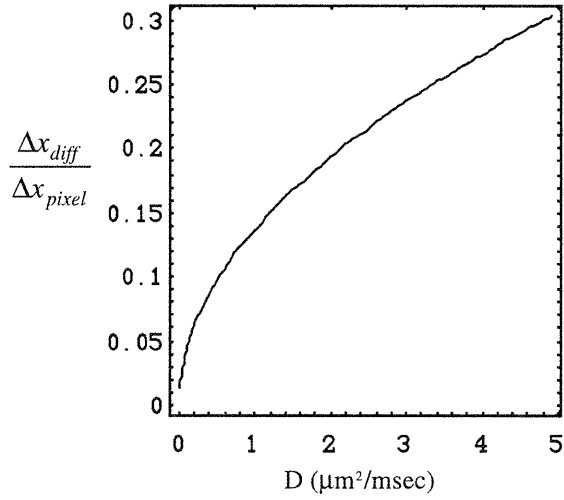
$$\begin{aligned} \Delta x_{diff} &= \sqrt{2DT_g}, \\ \Delta x_{pixel} &= 1/2k_{max}, \\ \Delta x_{diff} / \Delta x_{pixel} &= 2k_{max} \sqrt{2DT_g}, \end{aligned}$$

where T_g is the gradient on-time. While the parameter $\Delta x_{diff} / \Delta x_{pixel}$ measures the overall significance of diffusion in NMR imaging, its precise effect depends strongly on the imaging pulse sequence used.

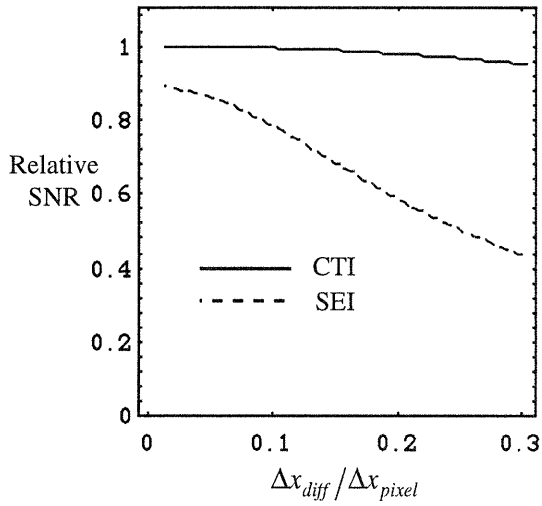
The sensitivity of 1D CTI was compared with that of 1D SEI as a function of the parameter $\Delta x_{diff} / \Delta x_{pixel}$. Since $\Delta x_{diff} / \Delta x_{pixel}$ depends on the pixel size, the diffusion constant of a sample, and the gradient on-time, the comparison was performed in two different conditions. First, the diffusion constant was varied while the pixel resolution was kept constant and second, the pixel resolution was varied while the diffusion constant was kept constant. Since the effects of the gradient on-time, which corresponds to the variation of gradient strength, was described in the previous chapter, it is not considered here. In CTI, the maximum gradient strength was assumed to be 1000 G/cm and, in SEI, the gradient strength was determined by matching the pixel bandwidth with the spectral bandwidth. The spectral bandwidth was taken to be 1 kHz.

The results for the first case is shown in Fig. 5-3, in which the pixel resolution is 5 μm and the diffusion constant is varied from 0.01 to 5 $\mu\text{m}^2/\text{msec}$. The parameter $\Delta x_{diff} / \Delta x_{pixel}$ increase with diffusion constant. As expected, the sensitivity of CTI is better than SEI in all ranges of $\Delta x_{diff} / \Delta x_{pixel}$. When $\Delta x_{diff} / \Delta x_{pixel}$ is small, the difference is small. However, as $\Delta x_{diff} / \Delta x_{pixel}$ increases, the sensitivity of CTI slightly decrease while that of SEI decreases appreciably, and so the ratio of the sensitivities, SNR_{CTI} / SNR_{SEI} , increases. This comes from the effectiveness of phase encoding to restrict the diffusional signal attenuation.

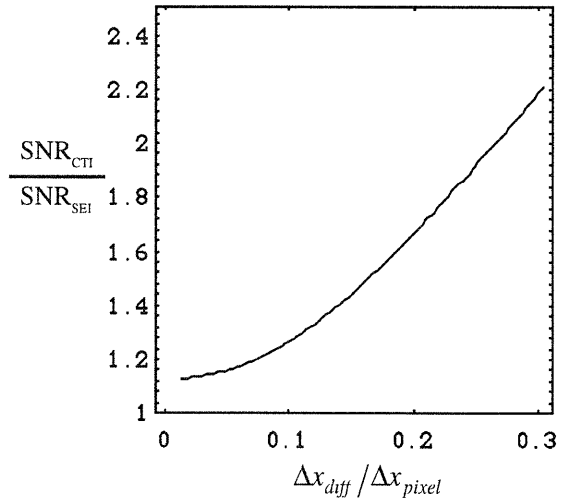
The results of the second case is shown in Fig. 5-4. The available number of spins is reduced with the voxel size, which consequently reduce the signal intensity. This affects both CTI and SEI equally, and so is not considered in this calculation. The diffusion constant is assumed to be 1 $\mu\text{m}^2/\text{msec}$ and the pixel size is varied from 1 to 20 μm . As the



(a)

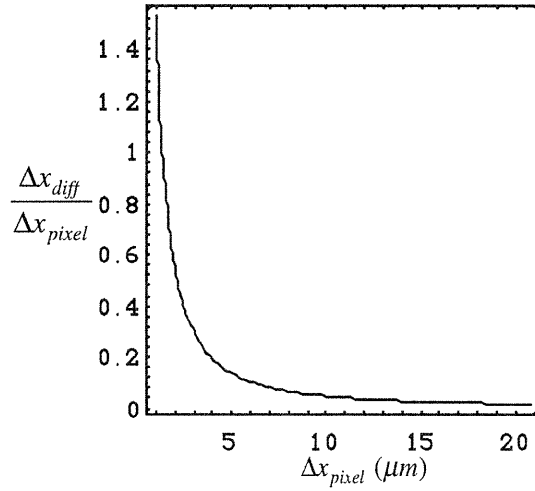


(b)

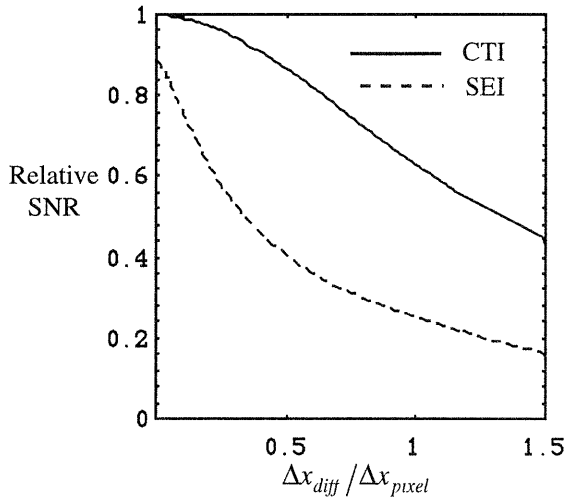


(c)

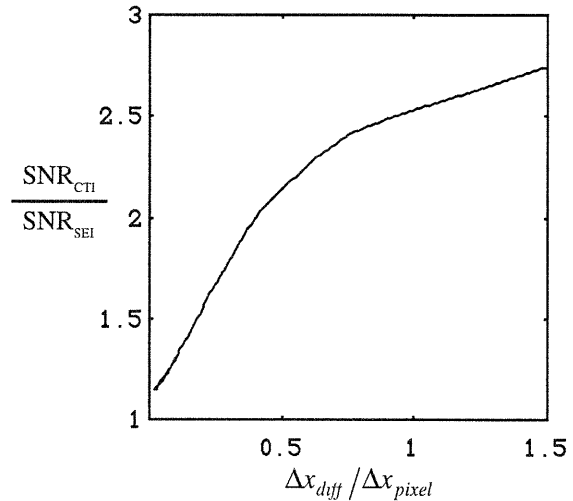
Figure 5-3. The sensitivity of CTI and SEI as a function of $\Delta x_{diff} / \Delta x_{pixel}$: Case 1. The diffusion constant is varied while the pixel size is kept constant. (a) $\Delta x_{diff} / \Delta x_{pixel}$ vs. diffusion constant, (b) relative SNR of CTI and SEI vs. $\Delta x_{diff} / \Delta x_{pixel}$, and (c) the ratio of SNR vs. $\Delta x_{diff} / \Delta x_{pixel}$. $\Delta x_{pixel} = 5 \mu m$, $T1 = 1$ sec, and $T2 = T2^* = 40$ msec.



(a)



(b)



(c)

Figure 5-4. The sensitivity of CTI and SEI as a function of $\Delta x_{diff} / \Delta x_{pixel}$: Case 2, the pixel size is varied while the diffusion constant is kept constant. (a) $\Delta x_{diff} / \Delta x_{pixel}$ vs. pixel size, (b) relative SNR of CTI and SEI vs. $\Delta x_{diff} / \Delta x_{pixel}$, and (c) the ratio of SNR vs. $\Delta x_{diff} / \Delta x_{pixel}$. $D = 1 \mu\text{m}^2/\text{msec}$, $T1 = 1 \text{ sec}$, and $T2 = T2^* = 40 \text{ msec}$.

pixel size decreases the parameter $\Delta x_{diff} / \Delta x_{pixel}$ increases dramatically. This shows how important molecular diffusion is in high resolution NMR microscopy. Although the sensitivities of both CTI and SEI decrease with $\Delta x_{diff} / \Delta x_{pixel}$, the ratio of the sensitivity of CTI to that of SEI increases with $\Delta x_{diff} / \Delta x_{pixel}$ i.e. as resolution becomes higher. This tells us that the effectiveness of CTI in restricting the diffusive signal attenuation compared to SEI is more pronounced as the resolution is improved.

As we can see from the results of the first and second cases, the sensitivity of CTI is always better than SEI. However, this does not mean that CTI is always a better choice than SEI. If the signal-to-noise ratio available in each signal averaging is large so that, in SEI, an $N \times N \times N$ image with an acceptable signal-to-noise ratio can be obtained by less than N signal averagings, the experiment time of SEI can be less than $N^3 \times T_R$. However, in CTI each signal averaging takes $N^3 \times T_R$, the experiment time is at least $N^3 \times T_R$. In this case SEI may be the better choice.

The minimum experiment time to acquire an image with a certain signal-to-noise ratio or better was calculated for the first case. In this calculation it is assumed that the required signal-to-noise ratio is less than the available signal-to-noise ratio in CTI by a single averaging and larger than that in SEI. Therefore, the experiment time of CTI is restricted by the total experiment time for a single averaging and is constant in this case. However, in SEI, the required signal-to-noise ratio can be matched by adjusting the number of signal averagings. Since the sensitivity of SEI decreases with $\Delta x_{diff} / \Delta x_{pixel}$,

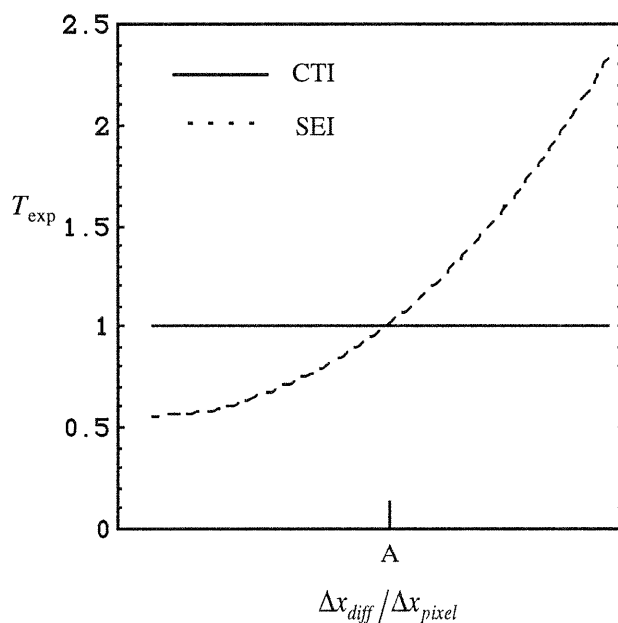


Figure 5-5. Minimum experiment time to achieve a certain signal-to-noise ratio.

the number of signal averagings increases with $\Delta x_{diff} / \Delta x_{pixel}$ and the experiment time also increases. These are shown in Fig. 5-5. Above the crossing point A, CTI takes less experiment time, and below A, SEI takes less. Therefore we may say that above A where the diffusion effects are more important, CTI would be better than SEI while below A where the diffusion effects are less important, SEI would be better than CTI. The position of crossing point A will depend on the required signal-to-noise ratio.

This argument can also be applied to the second case. Since $\Delta x_{diff} / \Delta x_{pixel}$ increase with the pixel size, we can infer that CTI would be the better choice in very high resolution NMR microscopy. The exact crossing point A may depend on several NMR parameters such as T_1 and T_2 as well as the diffusion constant of sample.

5.3 CPMG Sequence to Improve SNR

The signal-to-noise ratio in NMR experiment can be increased by signal averaging. However, this might not be desirable in CTI since each signal averaging takes a very long time. Here a way to improve the signal-to-noise ratio with a minimal experimental time is introduced.

A Carr-Purcell-Meiboom-Gill (CPMG) sequence^[5-5] is applied during the relaxation period of CTI, as shown in Fig. 5-6. The CPMG sequence is a series of π pulses and generates a series of echoes. Each echo peak corresponds to either +k or -k alternately because the π pulses switch the phase evolution by the phase encoding gradients. All echo peaks are collected, and the odd echo peaks (+k) and the even peaks (-k) are added separately. Therefore, the signal-to-noise ratio is enhanced in a single excitation. Since we only use the relaxation period, no additional experiment time is required in this method. Furthermore, the collection of both +k and -k in a single excitation may allow us to reduce the number of phase encoding steps required to collect the whole k space by half. Consequently the total experiment time is reduced by half.

The gain in the signal-to-noise ratio by CPMG sequence depends on the repetition time T_R , the number of π pulses during T_R , and the T_2 of the sample. The efficiency of the CPMG sequence in CTI is calculated for two different T_2 's and is shown in Fig. 5-6. In this calculation it is assumed that the whole phase encoding steps are used and the interval between π pulses is 4 msec. In both cases the maximum gain occurs when the total duration of CPMG is T_2 , and these gains are 3.3 for $T_2 = 100$ msec and 2.3 for $T_2 = 50$ msec. To achieve this gain in SNR by conventional signal averaging, the total experiment

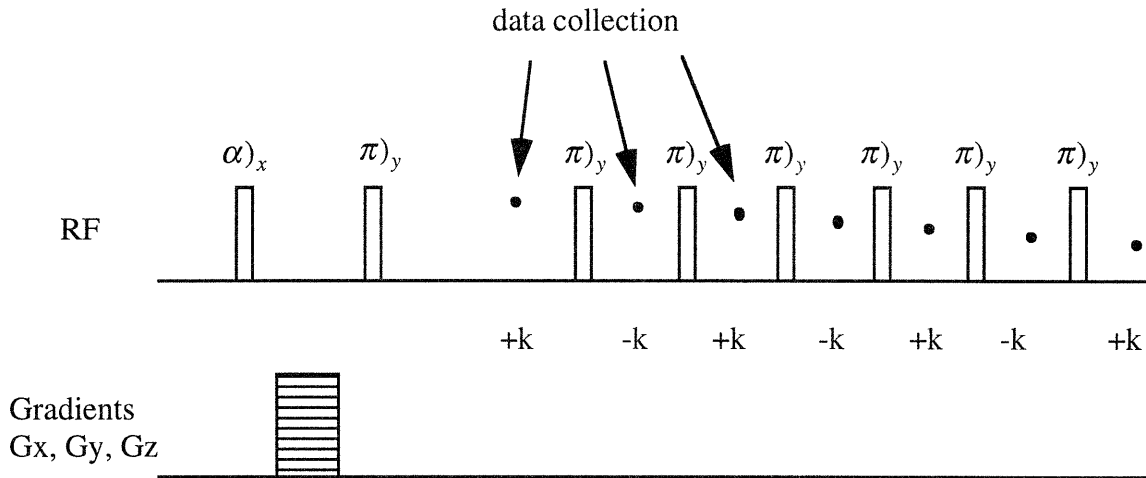


Figure 5-6. Pulse sequence for the optimized CTI. A conventional CTI is combined with CPMG sequence to allow multiple data collection. Data is collected at the center of each echo. The data points correspond to $+k$ or $-k$ alternately due to π pulses which switch the phase evolution due to the applied gradients.

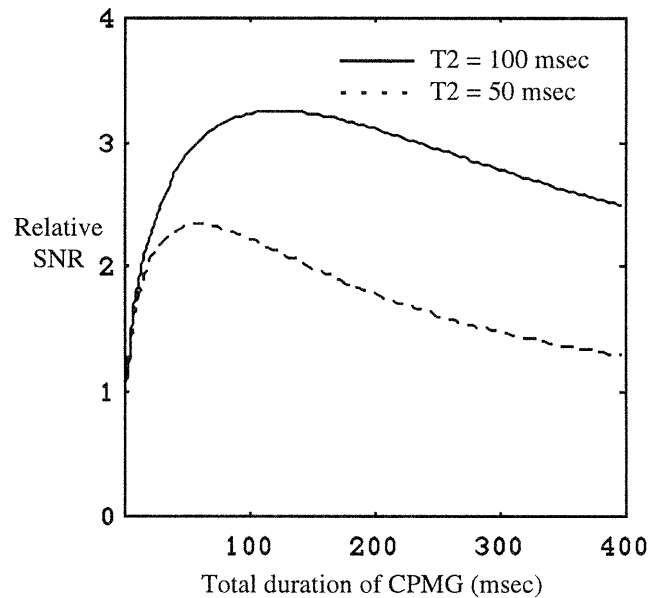


Figure 5-7. The efficiency of CPMG sequence in CTI as a function of the total duration of CPMG.

time would be increased by factor of 10 and 5 respectively. Therefore, the CPMG sequence has great potential to save experiment time in CTI.

5.4 Experiment Time in Constant Time Imaging.

In high resolution NMR microscopy, most experiments takes a long time to achieve enough signal-to-noise ratio to reconstruct an image. It was shown in the section 5.2 that CTI may be the better choice in very high resolution NMR microscopy. However, the long experiment time to acquire a single scan is still problematic. For example, when the repetition time T_R is 1 sec, an 3D image with 128 x 128 x 128 voxels takes about 24 days, which is not practical at all.

The problem may be overcome by using a shorter T_R and a smaller number of voxels. Some examples are given in table 5-1. If T_R is set 100 msec and the number of voxels are 64 x 64 x 64, the experiment time for a single scan becomes 7.3 hours, which is reasonable in high resolution NMR microscopy. However, there are penalties associated with this. Since the repetition time is determined by the T_1 relaxation time, the use of a shorter repetition time requires doping samples with relaxation agent to reduce T_1 . Such doping may require a very delicate skill process and may not be applicable to all samples. The repetition time is also restricted by the duty cycle of the gradient set since a fast repetition causes heating of the gradients. Second, the reduction of the number of voxels while keeping the resolution high reduces the FOV of the image. For example, an 64 x 64 x 64 image with a voxel size of 5 x 5 x 5 μm^3 has a FOV of 320 μm x 320 μm x 320 μm . However, since the main application of high resolution NMR microscopy may be at the cellular level, a small FOV may be acceptable. To decrease the total experiment time, we

Table 5-1. Examples of experiment time in constant time imaging.

| No. of data points | TR (msec) | Voxel size (μm^3) | FOV (μm^3) | Exp. time /scan (hr) |
|--------------------|-----------|-----------------------------------|---------------------------------|----------------------|
| 128 x 128 x 128 | 1000 | 5 x 5 x 5 | 640 x 640 x 640 | 582.5 |
| 128 x 128 x 128 | 100 | 5 x 5 x 5 | 640 x 640 x 640 | 58.2 |
| 64 x 64 x 64 | 100 | 5 x 5 x 5 | 320 x 320 x 320 | 7.3 |
| 256 x 256 | 100 | 5 x 5 x Δx_{slice} | 1280 x 1280 (μm^2) | 1.8 |

may also reduce the number of data points in one direction. One extreme example is to take a slice selected 2-D image rather than a 3-D image. In the slice selected 2-D imaging experiment, an image with a reasonably large inplane FOV can be acquired within relatively short experiment time.

Chapter 6

NMR Microscopy Probe Design

To implement the ideas discussed in the previous chapters, a strong gradient set and a sensitive RF receiver is required. A NMR microscopy probe for a standard bore Bruker AMX 400 MHz spectrometer was developed. This is equipped with a gradient set consisting of three orthogonal gradients with maximum strengths of 1000 G/cm for G_y , 1000 G/cm for G_z , and 250 G/cm for G_x , at 30 A, and an efficient small RF coil wrapped directly on a sample tube.

6.1 Strong Magnetic Field Gradient Set

In NMR imaging experiment the spatial grating of magnetization is generated by magnetic field gradients. Therefore, three orthogonal gradients $G_x(= \partial B_z / \partial x)$, $G_y(= \partial B_z / \partial y)$, and $G_z(= \partial B_z / \partial z)$ are required. As shown in the pervious chapters, these gradients need to be very strong to restrict the diffusional signal attenuation in high resolution NMR microscopy. In addition, the gradient set requires a fast switching time to allow a short strong gradient pulse, a uniform value in the imaging region to avoid image distortion and a minimal coupling with surrounding conductors to restrict eddy current.

The geometries of the coils for given gradient strength were determined based on a series of calculations : first by a series expansion method for idealized coils^[6-1] and then by Biot-Savart theory^[6-2] for actual coils. Based on these calculations, the strength, linearity, and efficiency of coils were known prior to construction of the coils.

In the gradient set developed in this research, the gradient coils G_y and G_z are quadruple coils and G_x is a Golay coil. The schematic diagram of current paths of the gradients are shown in Fig. 6-1. G_z has two current paths per quadrant at 30° and 60° positions and all current paths are connected by return paths which are not shown in the diagram. G_y is obtained by rotating G_z by 45° and G_x is a simple Golay coil with $K=0.40 R$, $K_r = 1.64 R$ and $\theta = 60^\circ$. The number of copper wires per each current path are 4 in G_z , 6 in G_y , and 4 in G_x and the wire diameter is 0.33 mm. The radius of the

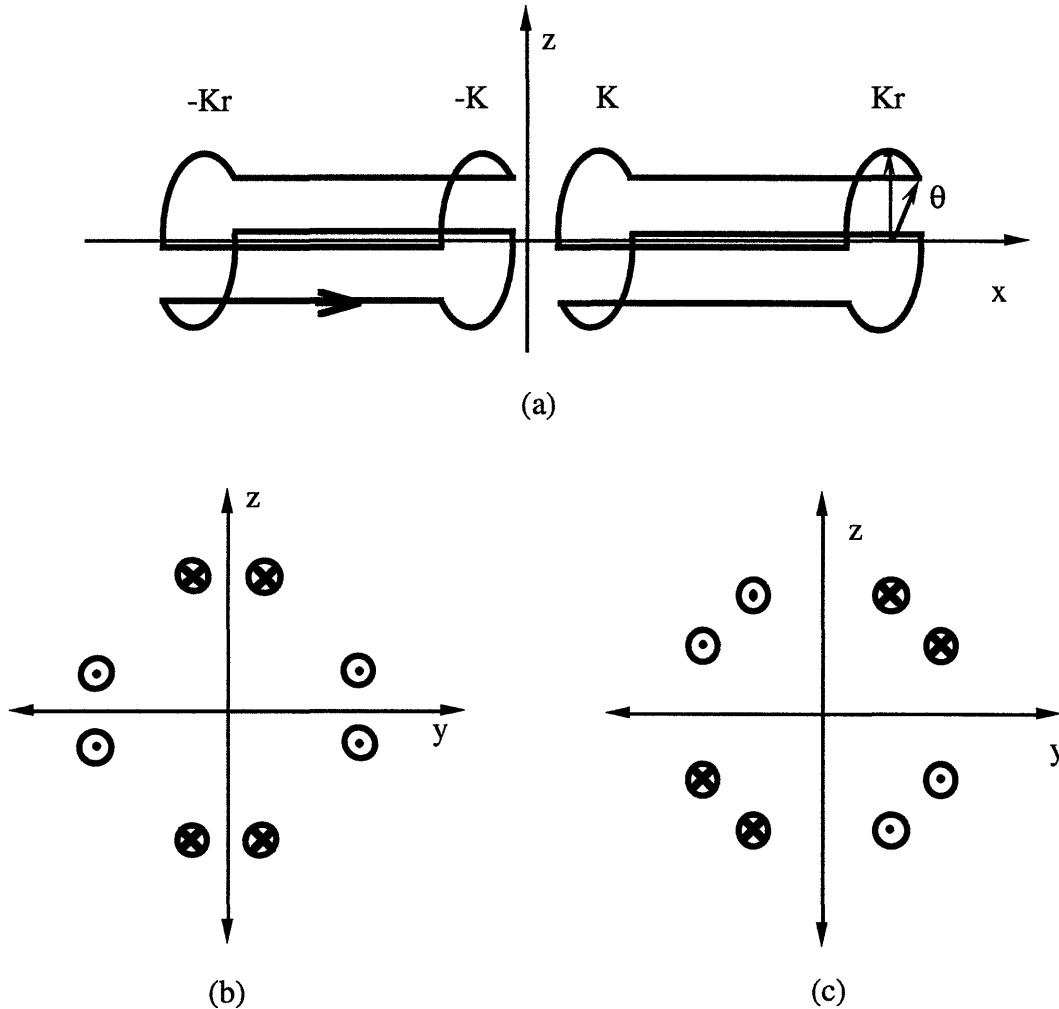
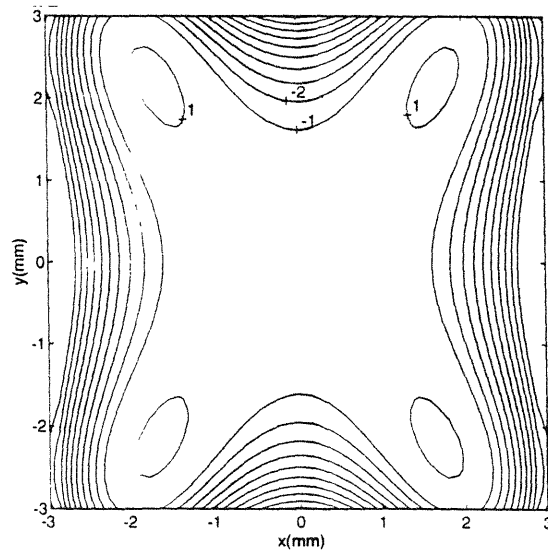


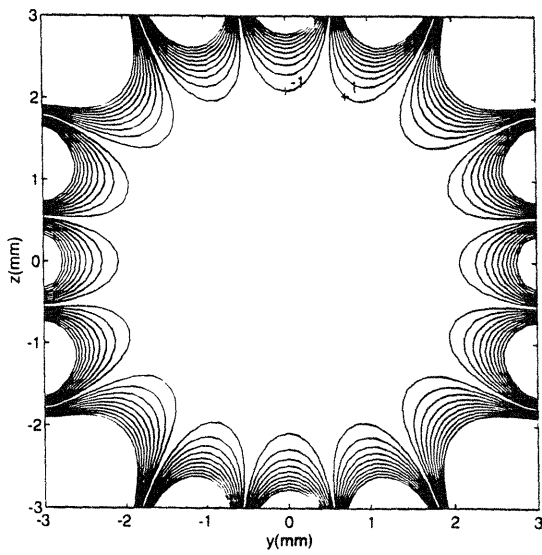
Figure 6-1. Schematic diagrams of current paths of x, y, and z gradient coils. (a) x-gradient is a Golay type coil, (b) y-gradient is a quadrupole coil, and (c) z-gradient is a quadrupole coil.

current paths, which is the distance from the origin of the axis to the bottom of the current paths, are 3.6 mm in G_z , 4.7 mm in G_y and 5.8 mm. The average length of the coils in the x-direction is about 17 mm. This relatively small size of the gradient set both increases the efficiency of the coils, and reduces eddy currents and inductive switching times.

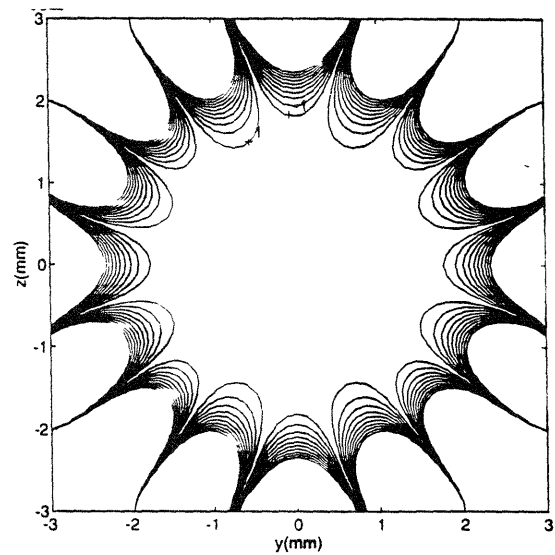
The calculated gradient strength of the coils are 1005 G/cm for G_z , 1017 G/cm for G_y , and 310 G/cm for G_x at 30 A. Fig. 6-2 shows contour plots indicating percentage deviation from these values. The radius of useful volume, which is defined as a region where the deviation is less than 1 %, is summarized in table 6-1.



(a)



(b)



(c)

Figure 6-2. Contour plots of percent deviation from the linear gradient at center. (a) x-gradient (x-y plane at $z=0$), (b) y-gradient (y-z plane at $x=0$), and (c) z-gradient (y-z plane at $x=0$)

Table 6-1 Radius of useful volume in gradient coils

| G_x | | G_y | | G_z | |
|--------|--------|--------|--------|--------|--------|
| z (mm) | R (mm) | x (mm) | R (mm) | x (mm) | R (mm) |
| 0.0 | 1.6 | 0.0 | 2.1 | 0.00 | 1.8 |
| 2.0 | 1.0 | 2.0 | 2.1 | 2.00 | 1.6 |

Table 6-2 Gradient strength and melting time.

| | G_x | | G_y | | G_z | |
|----------------------------|-------|-------|-------|-------|-------|-------|
| | Cal. | Meas. | Cal. | Meas. | Cal. | Meas. |
| Gradient at 30 A (G/cm) | 310 | 250 | 1018 | 1048 | 1006 | 1048 |
| Resistance (Ω) | 0.15 | 0.19 | 0.26 | 0.28 | 0.17 | 0.18 |
| Power at 30 A (W) | 135 | 171 | 234 | 252 | 154 | 162 |
| t_{melt} (sec) | 1.07 | - | 1.11 | - | 1.13 | - |

The gradient coils are wound on a 14 mm o.d. x 24 mm long cylindrical coil former that is transverse to the main magnetic field. Fig. 6-3 shows the detailed geometry of the former. The former is made of delrin and is machined by using a numerically controlled milling machine. The z gradient coil is placed in the inner most layer, the y gradient coil in the next and the x gradient coil in the outer most layer. For mechanical stability, the coils were fixed at position by Epoxy glue.

The strengths of the constructed coils were measured with 400 MHz imaging system at Bruker Instruments Inc. and compared with the calculated values, shown in table 6-2. They are well matched except in the x gradient. Since the coils are wound manually from inside to outside, there are certain errors in placing the wires at position as designed. This is most pronounced in the x-gradient which is placed at the outer most layer.

In fast repeating or long experiments which are the usual cases in NMR microscopy, the heating of the gradient set is one of the limiting factors. The resistance of each coil was measured and compared with calculated values. Based on these, the heat generation in each coil at current 30 A and the time for each coil to melt under a continuous power supply are calculated. In the calculation of the melting time it is

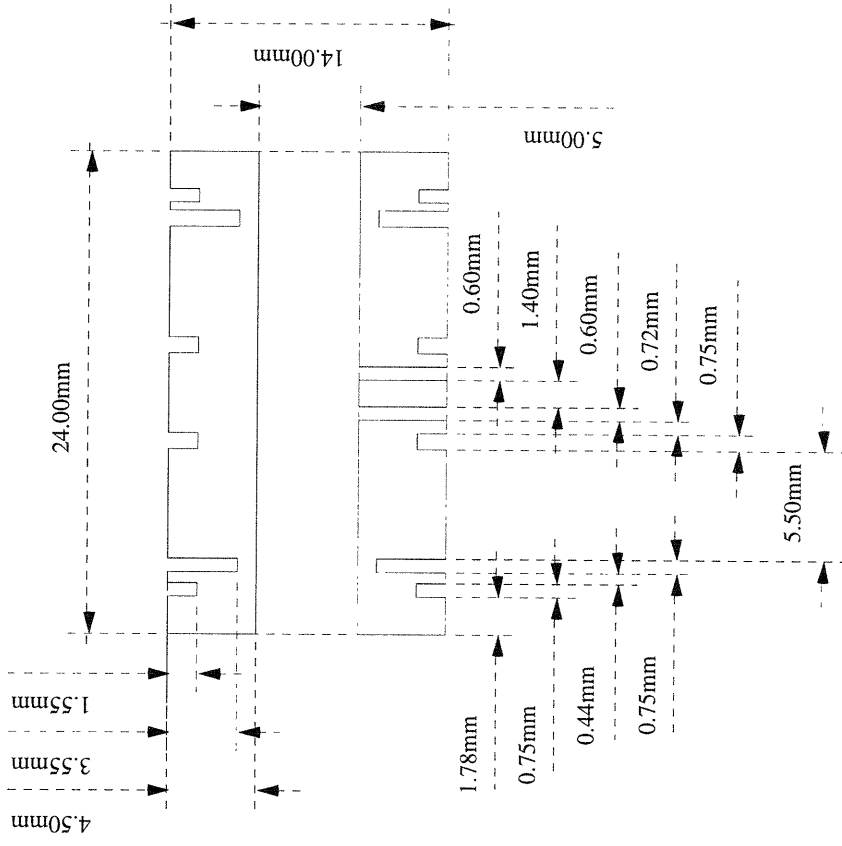


Figure 6-3. Drawing of a gradient former.

assumed that the generated heat is accumulated in coils with no heat transfer to surrounding. Although this calculation is crude, it provides an order of magnitude for time that we can turn on the gradient continuously. In practice, the gradients are applied as pulses on the order of 1 msec, and in most experiments the duty cycle of the gradient set is kept to less than 1 % for safety. To prevent the coils from melting during the experiment, a fuse is inserted into the power supply line of each coil.

6.2 Sensitivity of RF Micro Coils

In NMR microscopy, the signal is detected by the interaction between a sample and an RF coil, and the noise is dominated by the thermal noise in the coil. Therefore, the performance of the RF coil is directly related to the signal-to-noise ratio. The characteristics of the NMR receiver for large scale samples have been well investigated^[6-3], but most results are not appropriate for microscopic scale samples which requires small RF coils. Among different coil geometries(e.g. solenoidal, saddle, birdcage, and surface coils), solenoidal coil shows the highest sensitivity and are commonly used in NMR microscopy. The performance of solenoidal micro coils was investigated for two cases : first, given a sample volume and static magnetic field strength, the sensitivity of micro coils as a function of the number of turns in coils, and second, given a static magnetic field strength, the sensitivity as a function of coil diameter(i.e. sample diameter).

For a constant sample volume, by rearranging Eq. 3-9, the signal-to-noise ratio can be put into a simple form,

$$SNR \propto \frac{(B_1 / i)_{xy}}{\sqrt{R}}. \quad [6-1]$$

The geometry of solenoids is given in Fig. 6-4. In this calculation a cylindrical sample of length 2.0 mm and diameter 1.5 mm was used. This is the size which is appropriate for the NMR microscope developed in this research. Considering the finite thickness of sample tube, the diameter of the coil was assumed to be 1.7 mm plus the diameter of wires. The spacing between the wires were set at half of the wire diameter, which optimize the performance of each coil with respect to proximity effect, and the proximity effect was assumed constant in all coils. The resistance of each coil was calculated using Eq. 3-8 at room temperature and a static magnetic strength 9.41 T. $(B_1 / i)_{xy}$ is well known for solenoids,

$$(B_1 / i)_{xy} = \frac{\mu_o n}{D_c \sqrt{1 + (L_g / D_c)^2}} \quad n \gg 1, \quad [6-2]$$

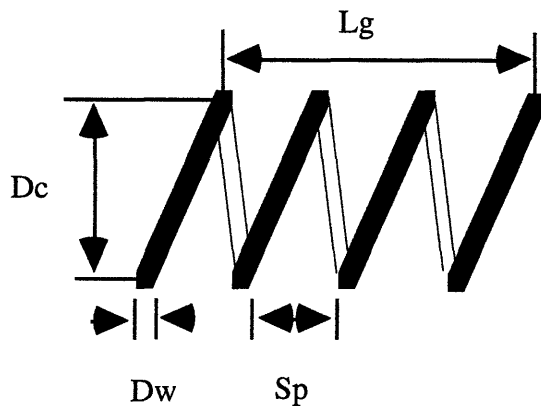


Figure 6-4. Geometry of a solenoidal coil.

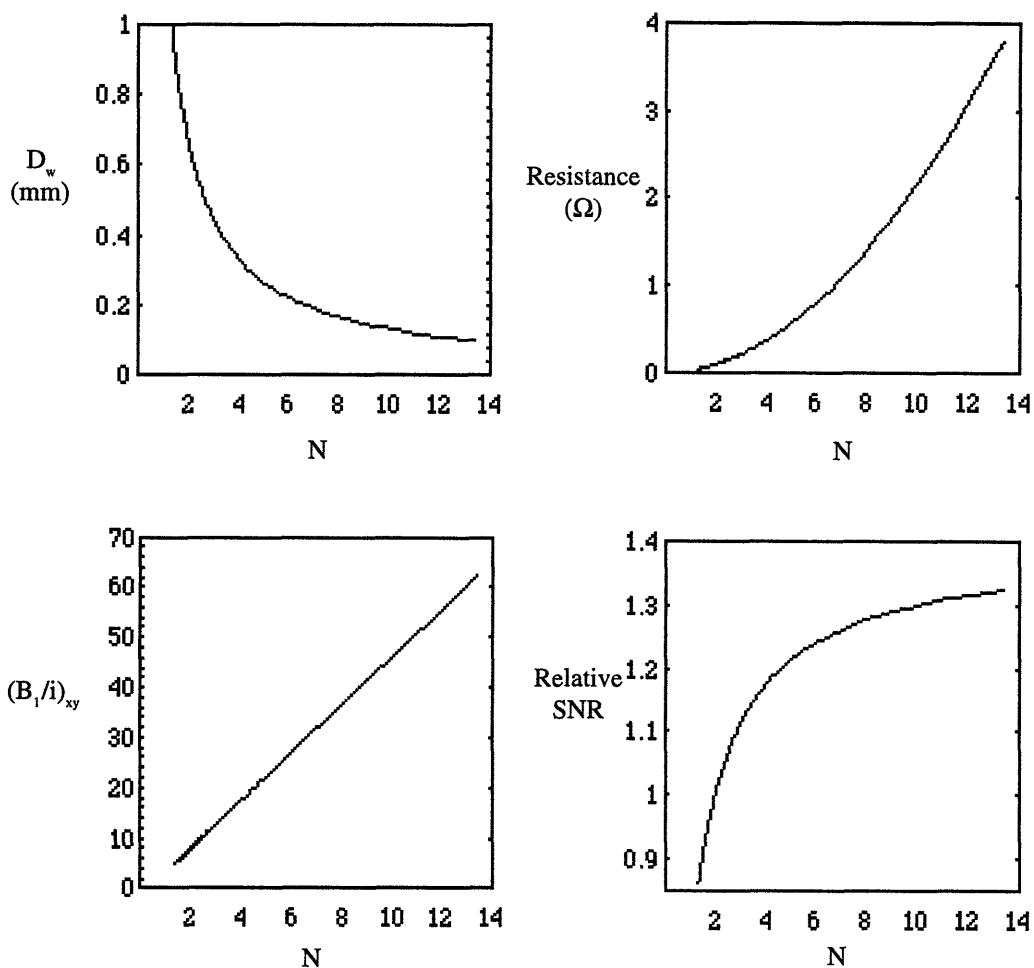


Figure 6-5. Sensitivity of micro coils for a constant sample volume. A cylindrical sample with diameter 1.5 mm and length 2.0 mm is assumed. As the number of turns, N , of solenoidal coil is increased, the diameter of coil decrease to fit in the fixed length of the sample. The relative SNR increases with N but, since the resistance of coil increase more rapidly than $(B_1 / i)_{xy}$, becomes saturated.

where μ_0 is the permeability of vacuum and n is a number of turns of coil.

The results are given in Fig. 6-5. As we increase the number of turns, the wire diameter decreases to fit in the given length of coil. $(B_1 / i)_{xy}$ increases with the number of turns but its contribution to the signal-to-noise ratio is compensated by the increase in resistance. Therefore, the relative signal-to-noise ratio increase with the number of turns and levels out at about $n=6$. The maximum gain in the signal-to-noise ratio is 35 % compared with the value at $n=2$. Considering that the proximity effects, which was assumed constant in this calculation, may be pronounced in the coils with more number of turns, the proper number of turns are between 5 and 8 for the sample volume considered here.

As we can see from Eq. 6-2, the sensitivity of signal detection is enhanced when the diameter of solenoids is reduced while maintaining the length-to-diameter ratio (L_g / D_c) constant. To properly understand the effects of coil diameter on the signal-to-noise ratio, the dependence of resistance on the coil diameter should also be considered. The sensitivity of solenoids with diameter 0.5 to 3.0 mm were calculated at 9.41 T and expressed in terms of the detectable number of spins. In this calculation the detection bandwidth was assumed to be 1 kHz. The detectable number of spins is defined as the number of spins which gives a unit signal-to-noise ratio in a single detection. Fig. 6-6 shows that the detectable number of spins decreases as the diameter of coil (sample) decreases. This tells us that as we decrease the diameter of coils we can detect a smaller number of spins and therefore can achieve a finer resolution. This agree with the results of others^[6-4,5,6].

As shown in Fig. 6-6, when the diameter of the sample is about 0.5 mm, the detectable number of spins is calculated to be 5×10^{14} . The measured value is 3.5×10^{15} spins with a 1.3 mm sample diameter. This value was obtained from an 3D SEI image with resolution $5 \times 5 \times 20 \mu\text{m}^3$ and detection bandwidth 25 kHz by assuming that the receiver bandwidth could be down to 1 kHz. As shown in the previous chapters, this narrow bandwidth is achievable using CTI. In the actual measurement, there are many noise sources other than the coil noise, and these make the difference between the measured value and the calculated value. If the extra noises are removed, the sensitivity will be much closer to the calculated value and we expect that the minimum detectable number of spins is about 2×10^{15} spins at 400 MHz with a 0.5 mm sample diameter.

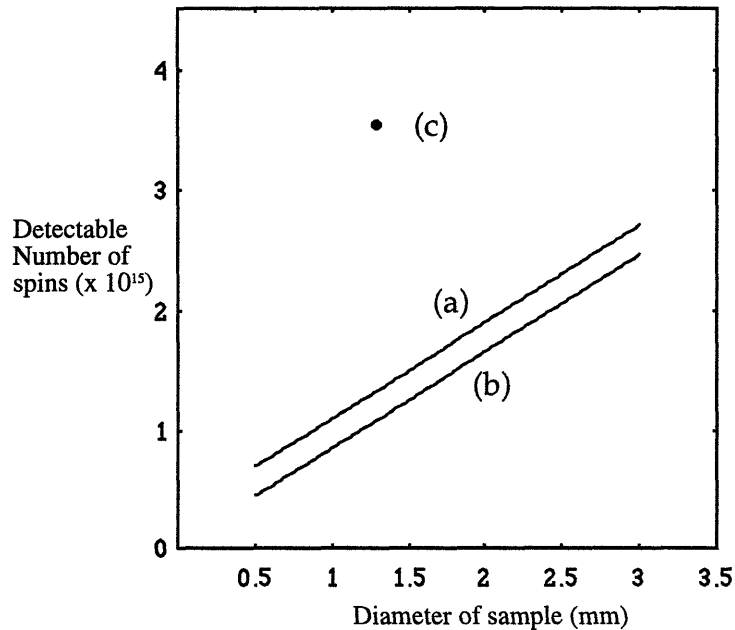


Figure 6-6 The detectable number of spins in a single excitation as a function of sample diameter at 9.41 T. Small solenoid RF coil is directly wrapped a sample tube. Diameter of wire used is (a) 0.5 mm , (b) 0.1 mm, and (c) 0.27 mm. (c) is a measured value with 3D spin-echo imaging.

6.3 NMR Microscopy Probe

A NMR microscopy probe on a standard bore (54 mm) Bruker AMX 400 MHz spectrometer was developed and its schematic diagram is shown in Fig. 6-7. Compared to commercially available NMR microscopy probes the probe has the unique features of much stronger and more efficient gradients, very high sensitivity RF circuits and a sample arrangement that is optimized for small tissue specimens.

The gradient set consists of three orthogonal gradients with maximum strengths of 1,000 G/cm for G_y , 1,000 G/cm for G_z , and 250 G/cm for G_x , at 30 A. The reduced efficiency of G_x compared with either G_y or G_z reflects the relatively simple coil geometry used, and is most useful for high resolution images with non-isotropic voxels. For pure water at room temperature, which has diffusion constant of $2.7 \mu\text{m}^2/\text{msec}$, a gradient strength of 1,000 G/cm is strong enough to virtually remove the diffusional signal attenuation at resolution as fine as $2 \mu\text{m}$. Considering that the diffusion constant of most biomedical samples is less than that of free water, the strength 1000 G/cm may be used for resolution higher than $2 \mu\text{m}$.

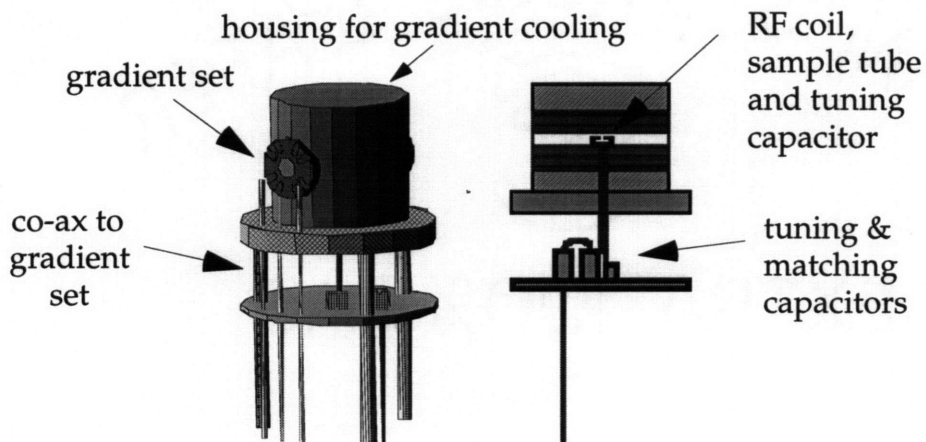


Figure 6-7. Schematic diagram of the NMR microscope probe. The sample is placed within a precision bore capillary tube and is then loaded into the gradient and RF coil set through a horizontal access hole. The RF coil is wrapped closely to the sample for good RF efficiency and the gradient set is kept small for high performance.

A small solenoid RF coil is placed inside of the gradient set and tightly wrapped around the sample tube. As shown in the previous section the signal-to-noise ratio per unit sample volume increases as the size of coil dimensions decrease. The inner diameter and length of RF coil is 1.7 mm and 2.0 mm respectively. The number of turns is 6 and the copper wire diameter is 0.27 mm. The size of the RF coil can be varied to accommodate other sample sizes. This design is appropriate given the small field of view and small samples that are encountered in microscopy.

Chapter 7

Representative Images and Application to Biomedical Research

At 400 MHz spectrometers, a series of images have been taken by using the NMR microscopy probe developed. Some representative images which experimentally show the ideas discussed in the previous chapters are presented in section 7-1 and the application to biomedical research is introduced in section 7-2.

7.1 Images of Water Phantom.

The resolution in NMR microscopy is limited by the available signal-to-noise ratio which is mainly determined by the size of the voxel and the diffusive signal attenuation. As the voxel size becomes smaller, the available number of spins decreases and the signal attenuation due to molecular diffusion in the presence of magnetic field gradient becomes very important, especially at resolution higher than 10 μm . As shown in the previous chapters, the diffusional signal attenuation can be reduced by using short intense gradient pulses.

The images in Fig. 7-1 shows the effects of voxel size and gradient strength on the signal-to-noise ratio. The sample is a doped water ($T_1 = 100$ msec) phantom containing fiber capillaries with i.d. 100 μm . To see the effects of the phase encoding gradient strength only, the detection bandwidth was kept constant 100 kHz. The total experiment time of each image was kept the same at 1 min. 17 sec. As the inplane resolution is changed from 14 μm x 14 μm to 7 μm x 7 μm , the signal-to-noise ratio is decreased by a factor of about 3 to 4, which is expected from the reduction of voxel size by a factor of 4. As the strength of maximum phase encoding gradient is increased from 100 G/cm to 1000 G/cm, in the images of 7 μm x 7 μm resolution the signal-to-noise ratio noticeably increases (by about a factor of 2). This shows the effectiveness of strong gradient reducing the diffusional signal attenuation. To achieve the same amount of improvement in the signal-to-noise ratio by signal averaging, the total experiment time must be increased by a factor of 4. The gain by using strong gradient is thus remarkable. However, in the

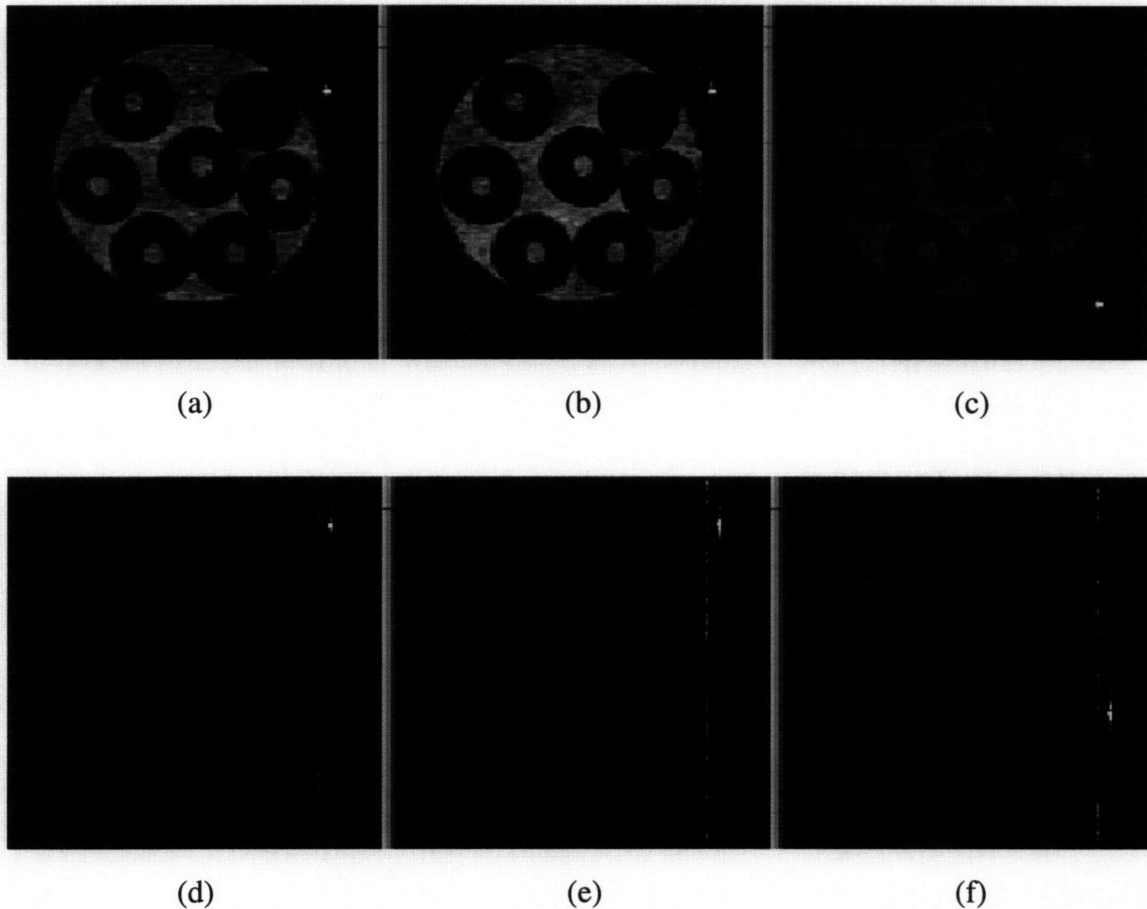
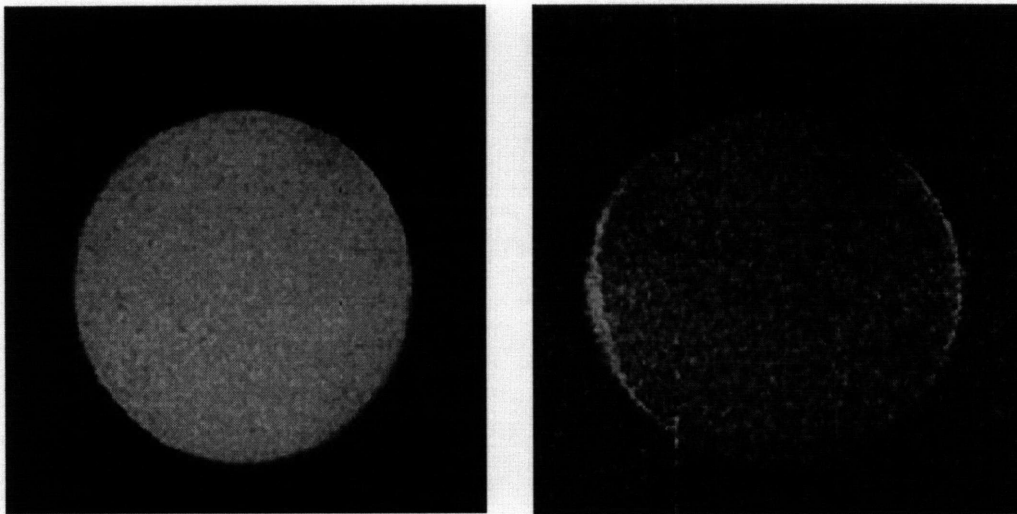


Figure 7-1 2D SEI images of a water phantom showing the effects of voxel size and gradient strength. Top three images(a, b, and c) have a inplane resolution $14\ \mu\text{m} \times 14\ \mu\text{m}$ with a slice thickness $200\ \mu\text{m}$ and bottom three (d, e, and f) have a inplane resolution $7\ \mu\text{m} \times 7\ \mu\text{m}$ with a slice thickness $200\ \mu\text{m}$. The maximum phase encoding gradient strengths are $1000\ \text{G/cm}$ (in a and d), $500\ \text{G/cm}$ (in b and e) and $100\ \text{G/cm}$ (in c and f). Each image was taken in 1 min. 17 sec with $\text{TR} = 300\ \text{msec}$. To keep the experiment time of each image same, top three have 2 averages and bottom three have 1 average. The signal-to-noise ratio of a, b, and c are 5.3, 5.3, and 4.6 respectively and that of d, e, and f are 1.9, 1.8 and ~ 1.0 .

images of $14\ \mu\text{m} \times 14\ \mu\text{m}$ resolution the improvement in signal-to-noise ratio is very small. This proves that molecular diffusion is important mostly at resolution beyond $10\ \mu\text{m}$.

When spins are confined to spatial regions by the presence of boundaries where the Brownian motion is impeded, the diffusive signal attenuation at the boundaries is reduced compared to bulk region. This leads to bright features at boundaries and is well illustrated in Fig. 7-2. The edge enhancement may be a useful information about local heterogeneity of sample.



(a) (b)
Figure 7-2 2D spin echo images of water filled in a tube with i.d. 1.3 mm. (a) The image was obtained with a read gradient 70 G/cm and TE = 6.73 msec, and shows uniform image intensity. (b) The image was obtained with a weaker read gradient 17.5 G/cm and a longer echo time TE = 27.09 msec allowing longer diffusion time. While the signal at unbounded region are attenuated by diffusion, the signal at the wall where molecular diffusion along the direction of the read gradient is restricted is preserved, showing bright crescent features.

It was shown in chapter 5 that constant time imaging is very effective in avoiding diffusional signal attenuation and may be the better choice especially when the total number of signal averagings required in spin echo imaging is larger than the number of data points along the frequency encoding direction. Fig. 7-3 shows a 2D 256 x 256 CTI image of a water phantom obtained in 5 hours and 30 minutes with a single average and a 2D 256 x 256 SEI image acquired in a same amount of time with 256 averages. Both images have a k-space limited inplane resolution $5 \mu\text{m} \times 5 \mu\text{m}$ with a slice thickness $200 \mu\text{m}$.

In the CTI image, the receiver bandwidth was set at 5 kHz and the maximum strength of phase encoding gradient was 1000 G/cm, which is strong enough to avoid the diffusive signal attenuation at $5 \mu\text{m}$ resolution. Therefore, as well as due to internal Hamiltonian and magnetic susceptibility, the point spread function due to diffusion is a delta function. In this case, the k-space limited resolution is a true resolution of the image. The image shows no distortion and allows us to clearly see the sharp features in the sample.

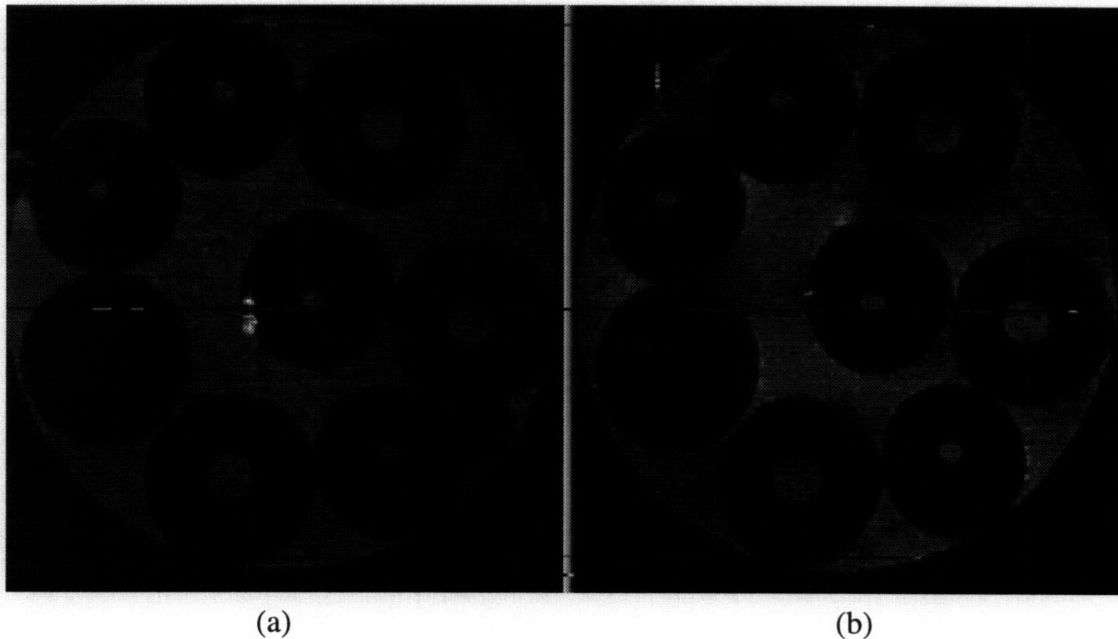


Figure 7-3 2D constant time image and 2D spin echo image of a water phantom containing fiber capillaries with i.d. $50\ \mu\text{m}$ and $100\ \mu\text{m}$. Both images were obtained in 5 hours and 30 minutes with $\text{TR} = 300\ \text{msec}$ and have a k-space limited inplane resolution $5\ \mu\text{m} \times 5\ \mu\text{m}$ with a slice thickness $200\ \mu\text{m}$ and FOV $1.28\ \text{mm} \times 1.28\ \text{mm}$. (a) Constant time image was obtained with a single average and a detection band-width $5\ \text{kHz}$ and has a signal-to-noise ratio 3.2. This is a very sharp image with no distortion (b) Spin echo image was acquired with 256 averages and a detection bandwidth $100\ \text{kHz}$, which is less than the optimal bandwidth. The signal-to-noise ratio is 3.5. This image is less sharp than a) and shows bright features, distortion due to magnetic susceptibility. The horizontal streaks in the images are artifacts induced during image data transfer.

In the SEI image, the receiver bandwidth was set at $100\ \text{kHz}$ (which corresponds to a read gradient of $180\ \text{G/cm}$) and the maximum strength of phase encoding gradient was $1000\ \text{G/cm}$. The receiver bandwidth was less than an optimal bandwidth at which each pixel covers the spectral width of the sample. Considering that the spectral bandwidth of the sample was about $1\ \text{kHz}$, the receiver bandwidth should have been set to $250\ \text{kHz}$. However, due to a practical problem in the NMR spectrometer, it was set at $100\ \text{kHz}$. Therefore, the true resolution of this image is lower than the k-space limited resolution. Considering the diffusive line broadening along the direction of read gradient, the actual resolution would be lower still. Therefore, the image shows less sharpness than the CTI image, and, furthermore, shows bright features at the outside boundaries of fiber capillaries

The signal-to-noise ratio of both images are about same (3.2 in the CTI image and 3.5 in the SEI image). However, considering that in the SEI image the improper setting of the receiver bandwidth enhanced the signal-to-noise ratio by a factor of $\sqrt{2}$ costing the true image resolution, at a same true resolution the signal-to-noise ratio of the CTI image is higher than that of the SEI image. This agrees with the theoretical prediction in chapter 5.

Two representative high resolution images of water phantoms are given in Fig. 7-4 and 7-5. These are among the highest resolution images published^[7-1,2,3].

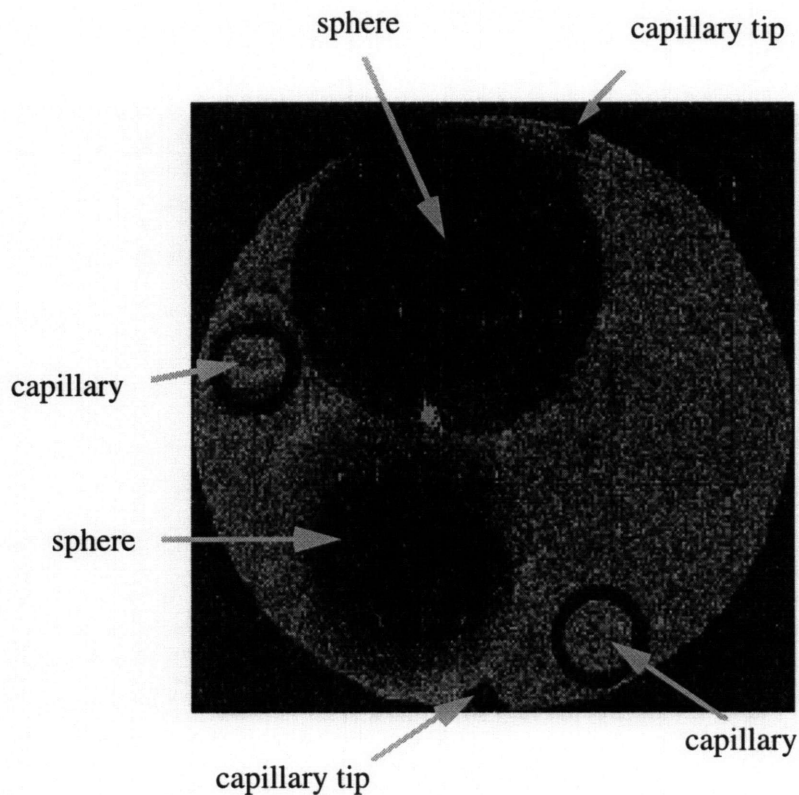


Figure 7-4 3D Fourier image of doped water ($T_1 = 100$ msec) in a phantom containing drawn two capillary tubes, two polystyrene spheres and two capillary tips. The image resolution is $5 \times 5 \times 20 \mu\text{m}^3$, with a field of view $1.28 \text{ mm} \times 1.28 \text{ mm} \times 320 \mu\text{m}$. The image was acquired in 18.2 hours with 10 averages and, $TR = 100 \text{ ms}$, $TE_{\text{grad}} = 829 \mu\text{s}$, and $TE_{\text{spin}} = 2.01 \text{ ms}$.

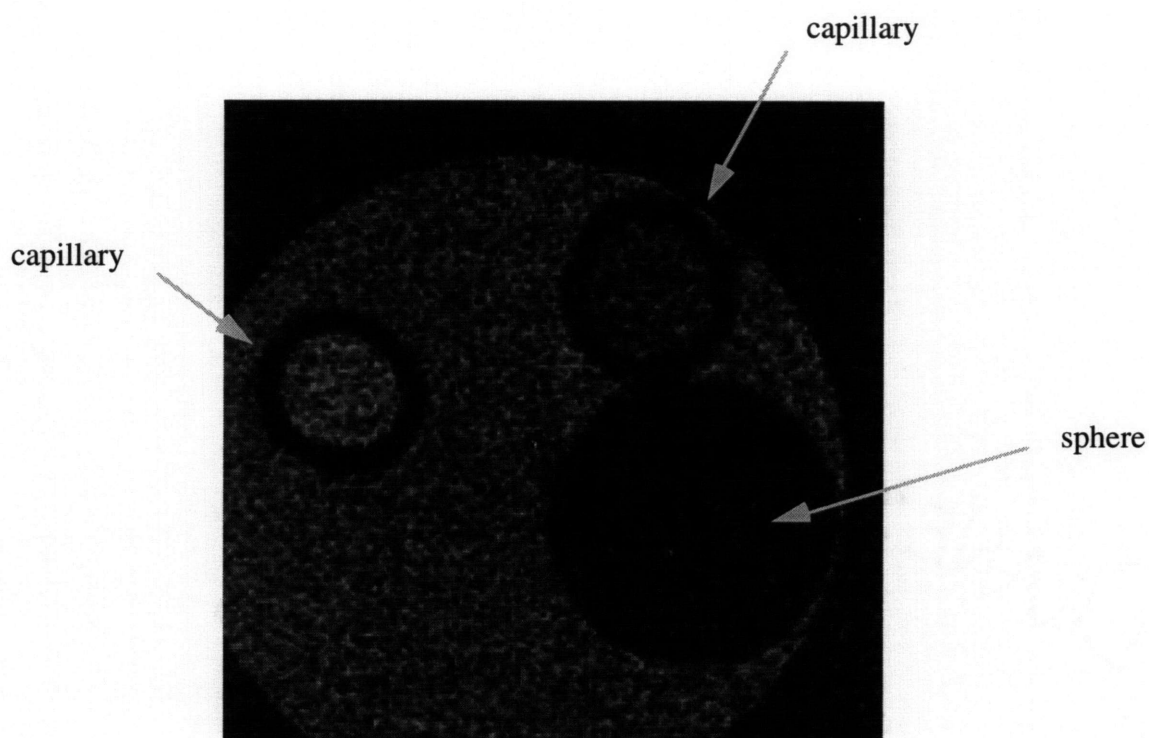


Figure 7-5 3D Fourier image of a doped water phantom ($T_1=100$ msec) containing two capillaries and one polystyrene sphere. The image resolution is $5\ \mu\text{m} \times 5\ \mu\text{m} \times 17\ \mu\text{m}$, with a field of view of $1.5\ \text{mm} \times 1.5\ \text{mm} \times 2.2\ \text{mm}$. The image was acquired in 4 hours with 2 averages and, $T_R = 80\ \text{ms}$, $T_E = 850\ \mu\text{s}$. The difference of signal intensity in capillaries and bulk water reflects differences in the relaxation times in the various regions corresponding to differences in the doping concentrations.

7.2 Application to Biomedical Research

Since NMR microscopy could provide information not easily obtained by other techniques, a successful NMR microscopy would have substantial value in biomedical research. Although its spatial resolution is poorer than conventional microscopy such as optical microscopy, NMR microscopy has two major advantages. First, it allows us to obtain three-dimensional information without sectioning, and second, image contrast can be based on a variety of NMR parameters such as proton density, spin-lattice relaxation time, spin-spin relaxation time, and diffusion coefficient. Therefore, NMR microscopy can complement traditional measurements in biomedical research by providing new information about local chemistry, morphology, and spin transport.

One great potential of NMR microscopy can be found in the rapid histological study of small excised tissue^[7-4]. The NMR microscopy probe developed in this research is quite appropriate for this purpose. Fig. 7-6 shows an example of NMR microscopy used for rapid histological studies performed in collaboration with SmithKline Beecham Pharmaceuticals. The images are of a healthy artery and an artery with atherosclerosis in which we can clearly distinguish the differences in artery wall thickness. This was acquired in only 28 minutes, and considering that in the past this information has been

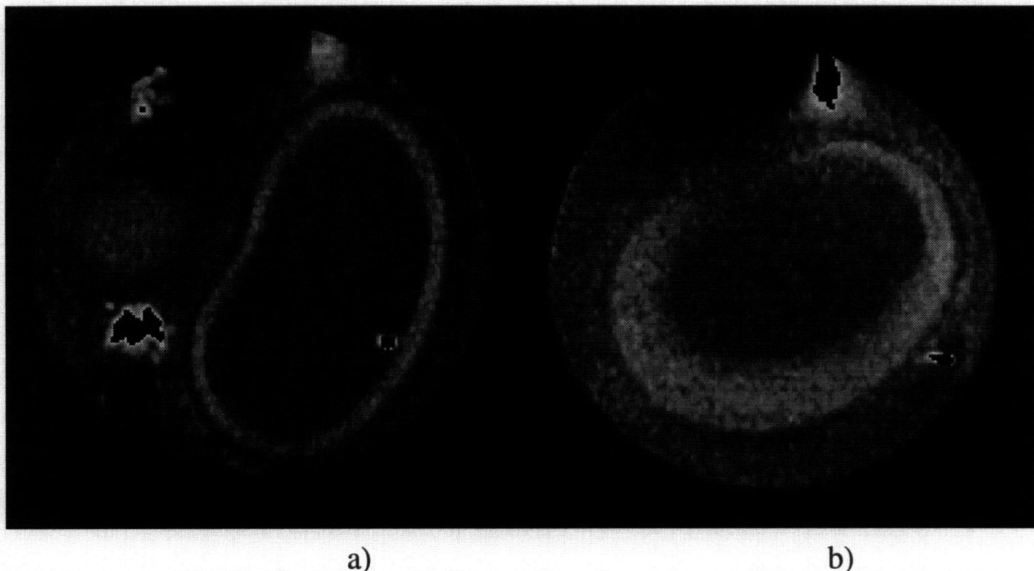


Figure 7-6 Images of a healthy rat artery a), and a rat artery with atherosclerosis b). The images were acquired using multi-slice 2D spin echo in 25 minutes with 8 averages, and have an inplane resolution of $13\mu\text{m} \times 13\mu\text{m}$ with a slice thickness = $200\mu\text{m}$. TE = 10 msec and TR = 1 sec. In the images we can clearly distinguish the differences in artery wall thickness.

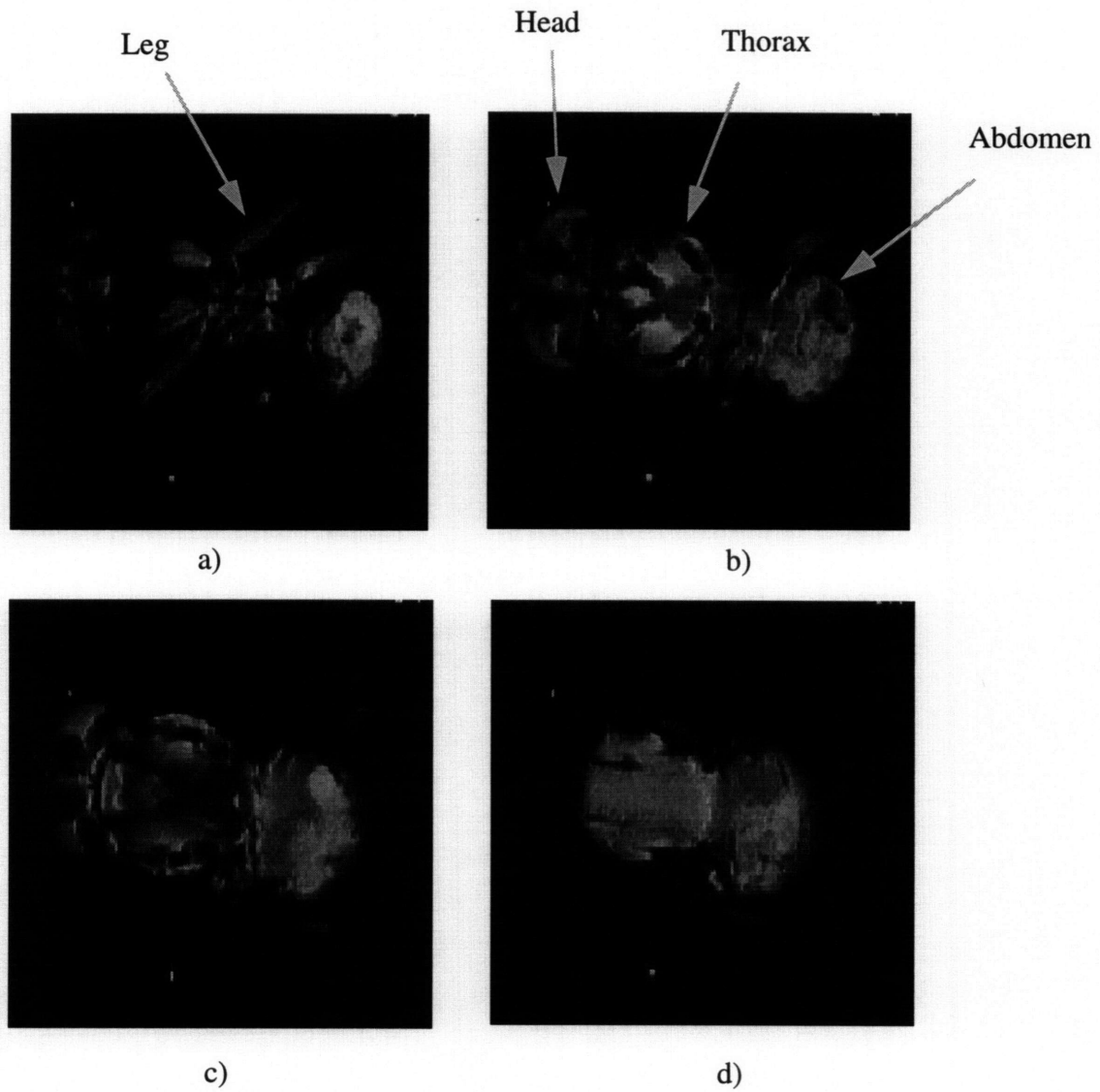


Figure 7-7 Images of a *Drosophila melanogaster* (adult fruit fly). The images were obtained using multi-slice 2D spin echo in 40 minutes, and have an in plane resolution of 20 μm x 20 μm with a slice thickness of 200 μm. a), b), c) and d) show the different slices from bottom to top.

obtained through labor intensive optical measurements, the usefulness of NMR microscopy is substantial.

The NMR microscopy probe is also appropriate for small living creatures such as *Drosophila melanogaster* which is one of the most favorite samples used in DNA research. Fig. 7-7 shows multi-slice 2D spin echo images of *Drosophila melanogaster*. The images were obtained in 40 minutes, and have an in plane resolution of $20\ \mu\text{m} \times 20\ \mu\text{m}$ with a slice thickness of $200\ \mu\text{m}$. In gene replacement research, the full three-dimensional information of gene replaced samples as a function of time is crucial to follow the development of the sample. NMR microscopy can possibly follow the development of gene replaced samples and identify the effects of gene replacement.

Chapter 8

Conclusion

It is widely accepted that a successful NMR microscopy would have a great impact on biomedical research. However, the prevailing opinion is that for practical applications the spatial resolution of image still must be improved. The limiting factors to the resolution of NMR microscopy images were discussed. Among those factors, molecular diffusion in the presence of magnetic field gradient is the most important at resolution higher than 10 μm . Molecular diffusion blurs the magnetization grating created by the gradient, reduces the signal intensity, and broadens the point spread function of a image. A way to avoid this problem was investigated. It was shown that the diffusive signal attenuation can be greatly reduced or avoided by employing strong magnetic field gradients. Using strong gradients, the gradient on-time can be very short and therefore, the diffusion time of spins during gradient pulse is reduced. However, the use of strong gradient increases the receiver bandwidth in frequency encoding detection and increases the thermal noise of an image. It was shown that constant time imaging, which use phase encoding in all directions, does not suffer this problem and be very effective to restrict the diffusive signal attenuation. Compared to spin echo imaging, constant time imaging can achieve a better signal-to-noise ratio within a given experiment time.

A NMR microscopy probe on a standard bore Bruker AMX 400 MHz spectrometer was developed, which has a very strong gradient set with maximum strength of 1000 G/cm at 30 A and a very efficient radio frequency receiver. The gradient strength of 1000 G/cm is strong enough to avoid molecular diffusion problem at resolution down to 2 μm . Using this probe the effects of gradient strength on the diffusive signal attenuation was measured and it agrees with the theoretical prediction. A constant time image with a resolution 5 μm x 5 μm x 200 μm was acquired and compared to a spin echo image with a same k-space limited resolution which was obtained in same experiment time. Considering the true resolutions of images, the constant time image shows a better signal-to-noise ratio and image quality. Some 3D images with high resolutions 5 μm x 5 μm x 17 μm and 5 μm x 5 μm x 20 μm were acquired and presented

The developed probe is quite appropriate for small excised tissues or very small creatures used in biomedical research. Some images of rat arteries and *Drosophila melanogaster* were acquired. These show the great potential of NMR microscopy as a powerful tool in biomedical research.

For further improvement of the resolution requires more research on the way to enhance the signal-to-noise of experiment. In the case of constant time imaging some gain may be achieved by applying a CPMG sequence during detection period. Signal averaging, one straight forward way of improving the signal-to-noise ratio, is limited by T_1 relaxation time of a sample. Considering all factors, the improvement of the resolution from 5 μm to 2 μm is not presently limited by the signal attenuation due to molecular diffusion but rather is limited by T_1 relaxation time of a sample, especially in a tissue sample. Therefore, the research on the control of T_1 relaxation time in tissues would make the achievable resolution one step closer to 2 μm .

References

- [1-1] E. M. Purcell, H. C. Torrey, and R. V. Pound, *Phys. Rev.* **69**, 37 (1946)
- [1-2] F. Bloch, W. W. Hansen, and M Packard, *Phys. Rev.* **70**, 474 (1946)
- [1-3] N. Bloembergen, E. M. Purcell, and R. V. Pound, *Phys. Rev.* **73**, 679 (1948)
- [1-4] P. C. Lauterbur, *Nature* **242**, 190 (1973)
- [1-5] P. Mansfield and P.K. Grannell, *J. Phys. C* **6**, L422 (1973)
- [1-6] P. Mansfield and P.K. Grannell, *Phys. Rev. B* **12**, 3618 (1975)
- [1-7] J. B. Aguayo, S.J. Blackband, J.Schoeniger, M.A. Mattingly, and M. Hintermann, *Nature* **322**, 190 (1986)
- [1-8] W. V. House, *IEEE Trans.on Nuc. Science* **NS-31**, No. 1, 570 (1984)
- [1-9] L. K. Hedges, 'Microscopic NMR Imaging', Ph.D. dissertation, SUNY at Stony Brook (1984)
- [1-10] P.T. Callaghan and C.D. Eccles, *J. Magn. Reson.* **78**, 1 (1988)
- [1-11] Z. H. Cho, C. B. Ahn, S. C. Juh, H. K. Lee, R. E. Jacobs, S. Lee. J. H. Yi, and J. M. o, *Med.Phys.* **15-6**, 815 (1988)
- [1-12] E.W. McFarland, *Magn. Reson. Imaging* **10**, 269 (1992)
- [1-13] C. P. Slichter, '*Principles of Magnetic Resonance*', Springer-Verlag (1990)
- [2-1] F.W.Wehrli, *Physics Today*, 34-42 June (1992)
- [2-2] S. Webb, '*The Physics of Medical Imaging*', IOP Pub. Ltd. (1992)
- [2-3] P.T. Callaghan, '*Principles of Nuclear Magnetic REsonance Microscopy*', Oxford Science Pub. (1992)
- [2-4] P.C. Laterbur, *Nature* **242**, 190 (1973)
- [2-5] P. Masfield and P.K. Grannel, *J. Phys. C* **6**, L422 (1973)
- [2-6] P. Masfield and P.K. Grannel, *Phys. Rev.* **12**, 3618 (1975)
- [2-7] R.R. Ernst, *Quart. Rev. of Biophys.* **19**, 3/4, 183 (1987)
- [2-8] P. Mansfield and P.G. Morris, '*NMR Imaging in Biomedicine*', Academic Press, Inc. (1982)
- [2-9] E.L. Hahn, *Phys. Rev.* **80**, 580 (1950)
- [2-10] C.P. Slichter, '*Principles of Magnetic Resonance*', Springer-Verlag (1990)
- [3-1] J.B. Aguayo, S.J. Blackband, J.Schoeniger, M.A. Mattingly, and M. Hintermann, *Nature* **322-6075**, 190 (1986)
- [3-2] R. W. Bowtell, G. D. Brown, P. M. Glover, M. McJury and P. Mansfield, *Phil.*

- Trans. R. Soc. Lond. A*, **333**, 457 (1990)
- [3-3] Z.H. Cho, C. B. Ahn, S. C. Juh, J. M. Jo, R. M. Friedenber, S. E. Fraser and R. E. Jacobs, *Phil. Trans. R. Soc. Lond. A* **333**, 469 (1990)
- [3-4] R. E. Jacobs and S. Fraser, *Science* **263**, 681 (1994)
- [3-5] S. Pauser, K. Keller, A. Zschunke and C. Mugge, *Magn. Reson. Imaging* **11**, 419 (1993)
- [3-6] Z. H. Cho, C. B. Ahn, S. C. Juh, H. K. Lee, R. E. Jacobs, S. Lee. J. H. Yi, and J. M. Jo, *Med. Phys.* **15-6**, 815 (1988)
- [3-7] C. D. Eccles and P. T. Callaghan, *J. Magn. Reson.* **68**, 393 (1986)
- [3-8] P.T. Callaghan and C.D. Eccles, *J. Magn. Reson.* **71**, 426 (1987)
- [3-9] P.T. Callaghan and C.D. Eccles, *J. Magn. Reson.* **78**, 1 (1988)
- [3-10] D. I. Hoult, *Progress in NMR Spectroscopy* **12**, 41 (1978)
- [3-11] A. Abragam, *Principles of Nuclear Magnetism*, Oxford Science Pub. (1961)
- [3-12] C.P. Slichter, *Principles of Magnetic Resonance*, Oxford Science Pub. (1992)
- [3-13] J. A. Kong, *Electromagnetic Wave Theory*, John Wiley & Sons, Inc. (1990)
- [3-14] D. I. Hoult and R.E. Richards, *J. Magn. Reson* **24**, 71 (1976)
- [3-15] B. B. Austin, *Wireless Eng. Exp. Wireless*, **11**, 12 (1934)
- [3-16] E. W. McFarland, *Magn. Reson. Imaging*, **10**, 269 (1992)
- [3-17] Z. H. Cho et al, *Phil. Trans. R. Soc. London A* **333**, 469 (1990)
- [4-1] W. V. House, *IEEE Transactions on Nuclear science*, **NS-31**, No. 1, 570 (1984)
- [4-2] P.T.Callaghan and C.D. Eccles, *J. Magn. Reson.***78**, 1 (1988)
- [4-3] W.B. Hyslop and P.C. Lauterbur; *J. Magn. Reson.* **94**, 501 (1991)
- [4-4] Z. H. et al, *Phil. Trnas. R. Soc. London A*, **333**, 469 (1990)
- [4-5] C.B. Ahn and Z.H. Cho; *Med. Phys*, **16-1**, 22 (1989)
- [4-6] W.B. Hyslop and P.C. Lauterbur, *J. Magn. Reson.* **94**, 501 (1991)
- [4-7] B.P. Hills, K.M. Wright, and P.S. Belton; *J. Magn. Reson.***8**, 755 (1990)
- [4-8] J.S. Schoeniger, N. Aiken, E. Hsu, and S.J. Blackband, *J. Magn. Reson.***B**, **103**, 261 (1994)
- [4-9] C. J. Rofe, J. Van Noort, P. J. Back, and P. T. Callaghan, *J. Magn. Reson.***B**, **108**, 125 (1995)
- [4-10] S. Singh and R. Deslauriers, *Concepts in Magn. Reson.* **7-1**, 1 (1995)
- [5-1] S. Emid and J.H.N. Creyghton, S. Emid and J.H.N. Creyghton, *Physica*, **128B**, 81 (1983)
- [5-2] D. G. Cory, *Ann. Rep. NMR Spect.*, **24**, 87 (1992)
- [5-2] S. Gravina and D.G. Cory, Sensitivity and resolution of constant time imaging

- [5-3] J. Link and J. Seelig, *J. Magn. Reso.* **89**, 310 (1990)
- [5-4] R. R. Ernst and G. Bodenhausen, and A. Wokaun, *Principles of Nuclear Magnetic Resonance in one and two dimensions*, Oxford Science Pub. (1994)
- [5-5] T. C. Farrar, *Introduction to Pulse NMR Spectroscopy*, The Farragut Press Chicago, Madison (1989)
- [6-1] Suits, B. H. and D. E. Wilken, *J. Phys. E: Sci. Instrum.* **22**, 565 (1989)
- [6-2] J. R. Reitz, F. J. Milford, and R. W. Christy, *Foundations of Electromagnetic Theory*, Addison-Wesley Pub. Co. (1979)
- [6-3] D.I. Hoult, *Progress in NMR Spectroscopy* **12**, 41 (1978)
- [6-4] D. L. Olson, T. L. Peck, A. G. Webb, R. L. Magin, and J. V. Sweedler, *Science* **270**, 1967 (1995)
- [6-5] R. W. Wiseman, T.S. Moerland et al, *NMR in Biomed.*, **6**, 153 (1993)
- [6-6] T. L. Peck, R. L. Magin, and P. C. Lauterbur, *J. Magn. Reson.*, **B 108**, 114 (1995)
- [7-1] X. Zhou, C. S. Potter, P. C. Lauterbur, and B. W. Voth, *Abstracts of the 8th annual Meeting of the Soc. Magn. Reson. in Med.*, 286, Amsterdam, The Netherlands (1989)
- [7-2] D. G. Cory and S. Gravina, *Bruker Reports*
- [7-3] E. McFarland, *Magn. Reson. Imaging* **10**, 269 (1992)
- [7-4] R. D. Kapadia, W. B. High, H. A. Soullveld, D. Bertolini, and S. K. Sarkar, *Magn. Reson. in Med.* **30**, 247 (1993)